UNIVERSITÀ DEGLI STUDI DI PADOVA

DEPARTMENT OF GEOSCIENCES

MASTER THESIS IN GEOPHYSICS FOR NATURAL RISKS AND RESOURCES

The use of Frequency domain Electro-magnetometer for the characterization of permafrost and ice layers

Supervisor: **JACOPO BOAGA**
Co-advisor: **MIRKO PAVONI**

Student: **MAHSA ASHRAF NAVIR**

Academic year

2022/2023

Acknowledgment

I want to extend my heartful thanks to Professor Boaga. His guidance and mentorship have been a constant source of inspiration for me. An iconic mentor whose busy schedule never prevented him from making time for his students. Teaching us the true essence of a mentor. There are no words to express my gratitude to him.

I also want to express my sincere thanks to Dr. Mirko Pavoni. Without his expertise and continuous support, even in his busy schedule, my research journey would not have been possible. His patience and dedication as a mentor have been truly remarkable and unforgettable.

I am profoundly grateful for the collaborative and nurturing environment within our department. My deepest and sincere gratitude to Professor Cassiani and Professor Ilaria Barone, who have had a profound impact on our development as geophysicists and have instilled in us a passion for learning. They will continue to be my role models throughout my career and life.

Lastly, I would like to thank my friends who tolerated me and supported me unconditionally, especially Jila Sharifi who has always been there for me in every moment. Without her constant support, I would not be where I am today.

Abstract

The Frequency Domain Electro-Magnetic (FDEM) technique holds great potential as a non-invasive and reliable method for characterizing and monitoring ice layers in high-mountain frozen environments. While methods such as Ground Penetrating Radar (GPR), Electrical Resistivity Tomography (ERT), and Refraction Seismic Tomography (RST) have been commonly employed in these settings, the FDEM method presents a novel and compelling alternative. Moreover, FDEM offers the distinct advantage of not requiring direct contact with the ground. Therefore, it facilitates a faster, more convenient investigation technique than other commonly used methods and could be a suitable solution for a wide range of environmental conditions, including frozen terrain in high mountains.

Furthermore, FDEM can be combined with other techniques to obtain a more detailed map of the subsurface. Inverted FDEM datasets are compared with other common methods to confirm FDEM's effectiveness. The results of this study provide new perspectives on FDEM's potential use in future paleoclimate studies and hazard assessments.

Contents

Introduction

Global warming refers to a long-term rise in the global average temperature. This warming trend has been going on for some time, but it has accelerated significantly in the last hundred years[1]. According to the European Environment Agency, the past decade has been the hottest decade on record [2].

Warming of the Arctic has resulted in an acceleration of permafrost and glacier degradation, making this region most vulnerable to climate change. The consequences of these changes, however, extend far beyond the Arctic boundaries. Therefore, it is critical to monitor changes in the ice layer thickness in high mountain areas. This is to minimize the risk of infrastructure destabilization and eventual future disasters[3].

Permafrost is frozen ground that remains at or below zero degrees Celsius for at least two years. It is found in mountains and polar regions and consists of frozen soil, sediments, or rock. As permafrost in the European mountain range is usually only a few degrees Celsius below zero, it is highly susceptible to climate change. Permafrost is composed of a relatively thin uppermost layer known as the active layer, which melts over the summer; if this layer becomes too deep or does not completely freeze during the winter, the ground may become unstable and pose numerous threats to both the ecosystem and the human society at large. Unlike the melting of glaciers, the degradation of permafrost is not immediately noticeable from the surface[4]. Therefore, monitoring the rate and magnitude of permafrost thawing throughout the years is essential [5].

Glaciers, crucial in regulating the Earth's climate, also serve as archives of invaluable information about past climates. By drilling deep into glaciers and extracting ice cores, scientists can analyze the composition of ancient air bubbles trapped in the ice [6].

These bubbles contain samples of the Earth's atmosphere from the time the ice formed. This provides insights into historical greenhouse gas concentrations and past climate conditions. Studying ice cores allows scientists to reconstruct temperature variations, atmospheric composition, and other climate parameters over centuries or even millennia [7].

Climate change has a significant impact on glaciers. Global warming has caused glaciers to melt at a faster rate. Therefore, it is critical to preserve ice cores for future research. Ensuring that valuable information about past climates and environmental conditions is preserved and made accessible to scientists and future research [7].

Despite the significance of monitoring glaciers and permafrost, accessing and investigating these remote and challenging environments pose considerable difficulties. However, recent advancements in remote-sensing technologies have greatly improved our ability to study these regions [8].

In this context, two distinct projects in the European mountain ranges, the Alps, and the Apennines, have been conducted. One of the aims of these studies was to analyze the advantages, disadvantages, and possibilities of using the Frequency Domain Electromagnetic (FDEM) method solo or integrated with other geophysical techniques in such geological contexts.

The first project aimed to study permafrost in the Sella Group mountains, Dolomites, Italy. Combining Electrical Resistivity Tomography (ERT) and FDEM (CMD-Explorer probe by Gf-instruments) it was possible to successfully identify the active layer thickness (ALT) and distribution of permafrost in two different mountains in the Northern Alp**s**, the Piz Boé and Murfreit mountains. The integration of these geophysical techniques provides a comprehensive understanding of permafrost dynamics. This offered crucial insights for monitoring permafrost degradation in the face of global warming that help scientists effectively manage natural hazards.

The second project, an international project known as “Ice Memory”, is focused on characterizing the Calderone Glacier in the Apennine Mountains, Italy. It aims to collect and preserve ice samples from vulnerable glaciers threatened by global warming. By integrating Ground Penetrating Radar (GPR) and separated-coils FDEM (CMD-DUO, GF-Instruments) techniques we were able to identify the optimal location for ice coring (the location of the ice core with greatest ice thickness). This innovative approach demonstrated the potential of FDEM as a valuable method for glacier environment studies.

Case studies Site Description

This thesis is focusing on two distinct investigation sites located within the Alpine and Apennine Mountain ranges. In this section, a comprehensive and detailed description of the researched locations is provided, as well as an exploration of the historical context of glaciers in the study areas.

Geomorphology and Geographic Context of Sella Group Mountain

The Sella Mountain chain is an alpine plateau-shaped mountain group with an average elevation of 2,500 m (8,202 ft) in the Dolomites in northern Italy. Situated North-east of the Marmolada and in the east of the Gruppo Sassolungo as well as between Val di Fassa (Trentino), Livinallongo (Belluno), Val Gardena, and Val Badia (South Tyrol).

Figure 1.*SELLA GROUP MOUNTAINS*

The plateau of the Sella Group exhibits a Tundra climate, signifying a local climate in which at least one month has an average temperature high enough to melt snow (0 °C), but no month with an average temperature in excess of 10 °C. it means that the average temperatures rise above 0°C exclusively during the summer season. July gets the most rain, around 130-135 mm. In autumn, snow falls, making a good base for winter. Temperatures are a bit colder than the Western Alps but warmer than the Eastern Alps. January and December are the coldest months, while July and August are the hottest. Sometimes, even during the summer, there may be snowfall due to very cold air. The weather data on the Piz Pisciadú station, from 2004 to 2020 indicates summer temperatures ranging between +3°C and +5°C, while winter temperatures range from -8°C to -10°C.

The peaks of the Murfreit group are situated on the northernmost part of the Sella massif west of the Rifugio Pisciadú in the Dolomites [9] for a total area of 0.34 km^2 with lobate shape rock glaciers of 1100 m of width and an overall length of 420 m. It has an elevation of 2590 meters on the rock glacier, with a 2770 m heigh rooting zone [5].

In the north-northwest direction of the Sella group, the rock glacier is exposed on the surface. However, in the southern part, the Sella platform holds steeply inclined slope deposits composed

of the “Dolomia Principale” formation cut by several steep faults that are covered with debris [5]. Therefore, the rock glacier is entirely composed of dolomite debris. Due to the steep terrain near fault zones, rockfalls are common in this area [10].

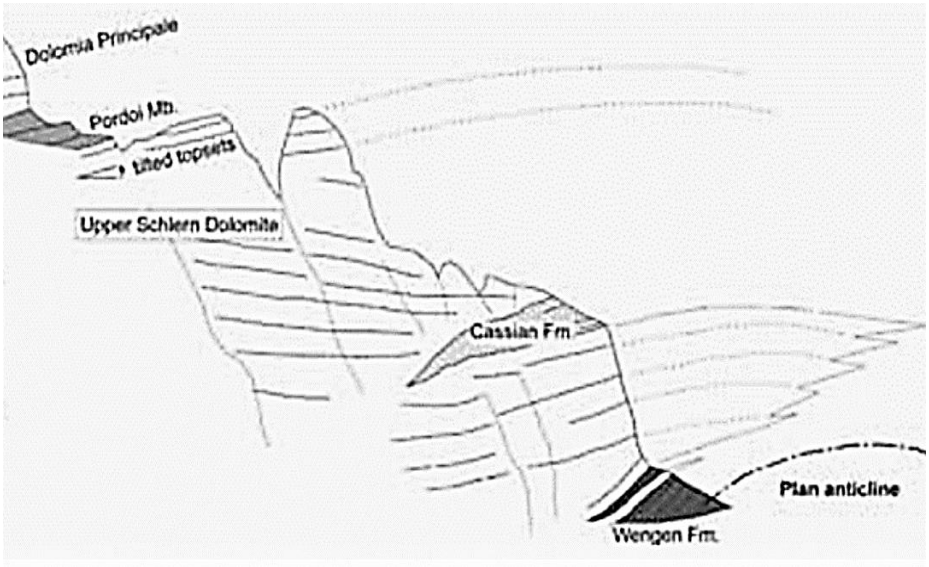

***Figure 2**: The stratigraphic relations at Murfreit (according to Keim’s interpretation).*[10]

In the northern region of the Sella Group, ten glaciers exist, covering a total area of 0.54 square kilometers. These rock glaciers were categorized into four active, five inactive, and one relict types. Active rock glaciers are less likely to be found in mountain ranges with carbonate rock, such as the Northern Calcareous Alps and the Dolomites. Among active rock glaciers in sella mountain, Murfreit stands out as the most extensive and most active one. Another adjacent rock glacier, known as Sas Dala Luesa, is situated to the east of Murfreit. Both of these rock glaciers are positioned on the prominent Raibl terrace, which itself is located west of Rifugio Pisciadú [11].

***Figure 3**: A view of Rock Glacier Murfreit from the North.*

Due to the steep terrain near fault zones, rockfalls are common in this area. In the summer of 2003, the Sella Group experienced multiple debris flows due to heavy rainfall and a thunderstorm. These flows blocked the road from Wolkenstein to Gröden Pass, with the most significant one occurring on July 2, when a debris flow from the rock glacier Murfreit obstructed the road. Additional debris flows occurred in the area during this period, including one in the Culea Valley on July 23 and two smaller ones on July 24, all affecting the road to Gröden Pass.[11]

As a result, it is crucial to conduct in-depth studies of the rock glaciers in this region, as their dynamics and potential for triggering debris flows have significant implications for the safety and infrastructure of the area.

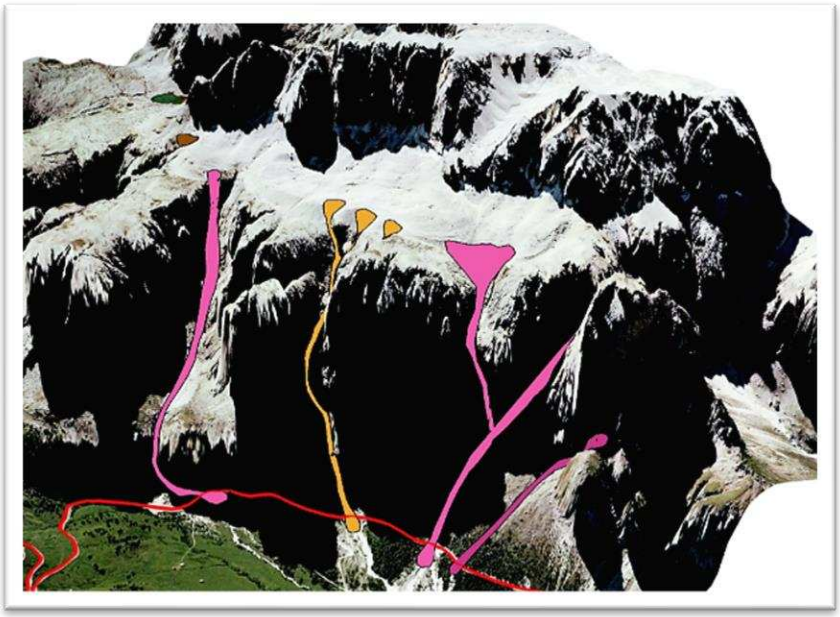

Figure 4*.Panoramic view on the northern part of the Sella massif with rock glacier Murfreit. Debris flows were initiated from the steep front of the rock glacier terminating at the edge of the terrace. As the rock glacier is still active in the western part, debris flows may be initiated there during heavy rainfall events (Mussner, 2010). Pink: debris flows of summer 2003, light and dark brown: additional potential areas for the formation of debris flows. The red line marks the road to Gröden Pass.*[11]

Proceeding towards the South-east of the Sella Group, we reach the Piz Boé mountains.

The Piz Boé is the highest summit of the Sella Group (3152 m) located on its South-eastern side (46°30'N, 11°50'E). Rock glaciers in this area extend for an average altitude of approximately 2900 meters and are surrounded by a system of low-angle thrust.

Similar to Murfreit, Piz Boé consists primarily of the "Dolomia Principale" formation and additionally of limestone of the "Dachstein" formation. As a result, the rock glacier debris in this area is calcareous and dolomitic.

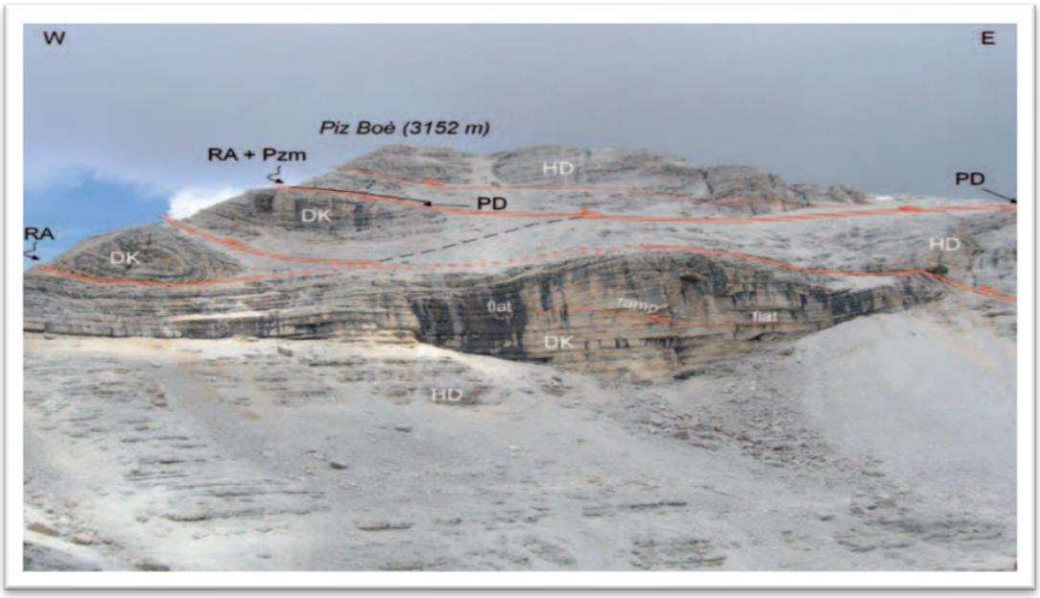

***Figure 5**: Line drawings of the southern Piz Boé PD = Pordoi Fm, HD = Dolomia Principale, DK = Dachstein Limestone* [12].

In the north-East region of the Piz Boé peak, a glacier was present during the 1980s survey, which occupied an approximate area of 0.04 km2. However, the current extent of glaciated terrain is significantly reduced, measuring around 0.014 km2. Beneath this receding glacier, a debris-covered expanse has developed, sometimes categorized as a rock glacier on certain maps.

The formation of Sella group

The Sella Group, like the rest of the Dolomites, has its origins in a marine environment. Around 280 million years ago, during the Permian period, the area that now comprises the Dolomites was submerged under a shallow sea. Over time, the accumulation of marine organisms, particularly coral reefs and microorganisms, formed layers of limestone.

During the Mesozoic era, which spans from about 252 to 66 million years ago, tectonic forces began to shape the region. Subsequent processes of deformation and uplift began around 10-20 million years ago, and the uplift of the ancient sea floor and subsequent exposed the limestone

formations that we see today in the Dolomites, including the Sella Group. The distinctive jagged peaks and steep cliffs that characterize the Dolomites are a result of this geological history.

Furthermore, during the Oligocene and Miocene epochs (around 34 to 5 million years ago), the Dolomites experienced further tectonic activity, including the collision of tectonic plates and the uplifting of the mountain ranges. Glacial erosion during the Pleistocene epoch, which began about 2.6 million years ago and lasted until around 11,700 years ago, also played a significant role in shaping the landscape, creating U-shaped valleys and cirques that are common features in the region.

Geophysical investigation in alpine mountains (The Sella group)

During the summer of 2020, the research was conducted in the active rock glaciers of the Sella mountains.

In the following image, we can see the investigation line in this area that extended 70.5 meters longitudinally along the Murfreit rock glacier.

***Figure 6**: Murfreit Rock Glacier* [5].

The investigation line on Piz Boé's rock glacier was established orthogonally to the direction of the rock glacier development with the same length of 70.5 meters.

***Figure 7**. Piz Boé rock glacier.*

Geomorphology and Geographic Context of Calderone glacieret

The Apennine Mountain range extends approximately 1,200 kilometers (746 miles) from the northwest to the southeast of Italy. They divide the country into different regions with distinct climates. The western side of the Apennines tends to be steeper and more rugged, while the eastern side slopes more gently towards the Adriatic Sea.

Corno Grande, meaning "The great horn" in Italian, is the tallest mountain in the Apennine Mountains located in central Italy, in the region of Abruzzo between the Provinces of L'Aquila and Teramo. It is entirely formed by calcareous Triassic platforms [13].

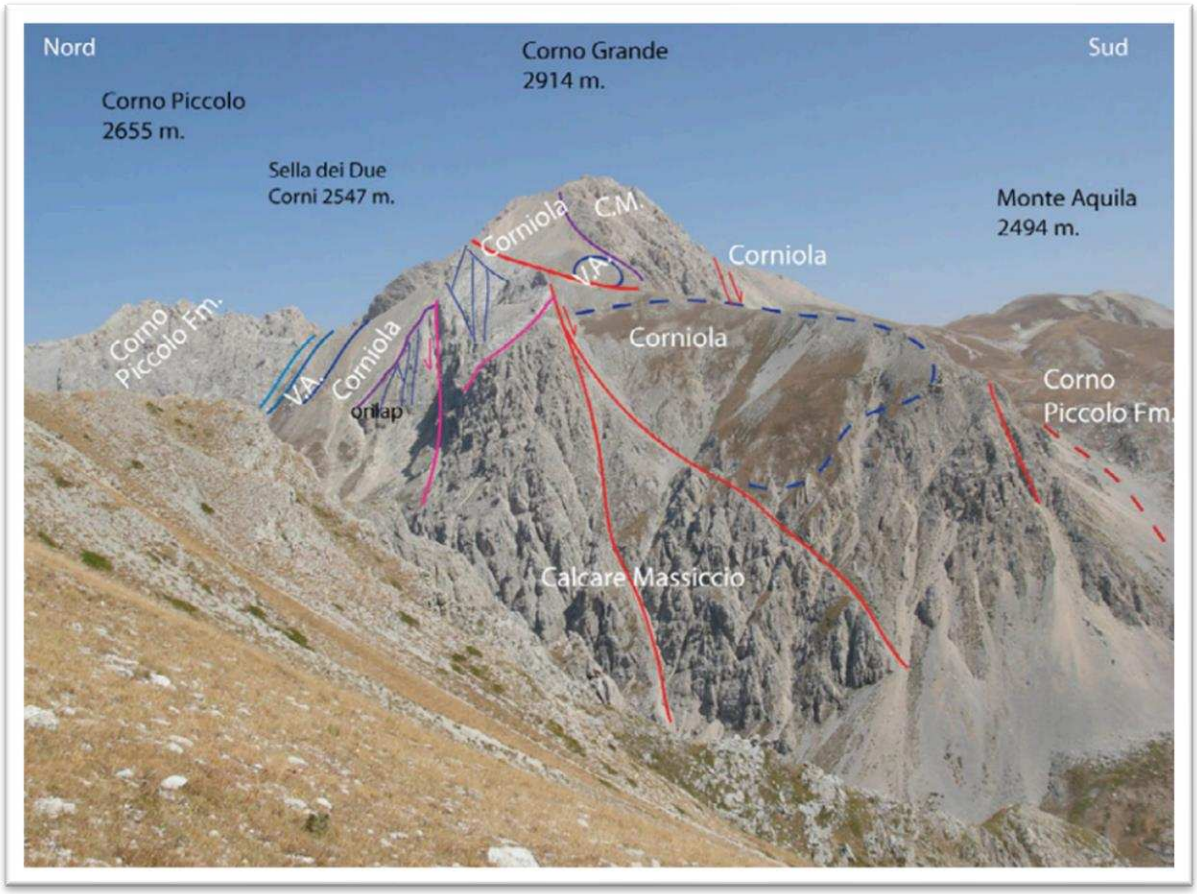

***Figure 8**: Panoramic photo of the geological setting of Corno Grande-Corno Piccolo* [13].

Corno Grande forms part of the Gran Sasso massif and stands as the highest peak of the Apennines, and the second-highest mountain in Italy outside the Alps. It reaches an elevation of 2,912 meters (9,554 feet). the north side of Corno Grande has steep slopes, while its south side is less elevated compared to the nearby Campo Imperatore plateau.

On the northern slope of the Corno Grande, you can find the southernmost glacier in Europe, known as the Calderone Glacieret. the Calderone Glacier has been shrinking over the years due to the effects of global warming and changing climate conditions. The glacier has experienced a considerable reduction in size and thickness. (I will discuss further in the 'History of Glaciers in the Alps and Apennines' section in this chapter.)

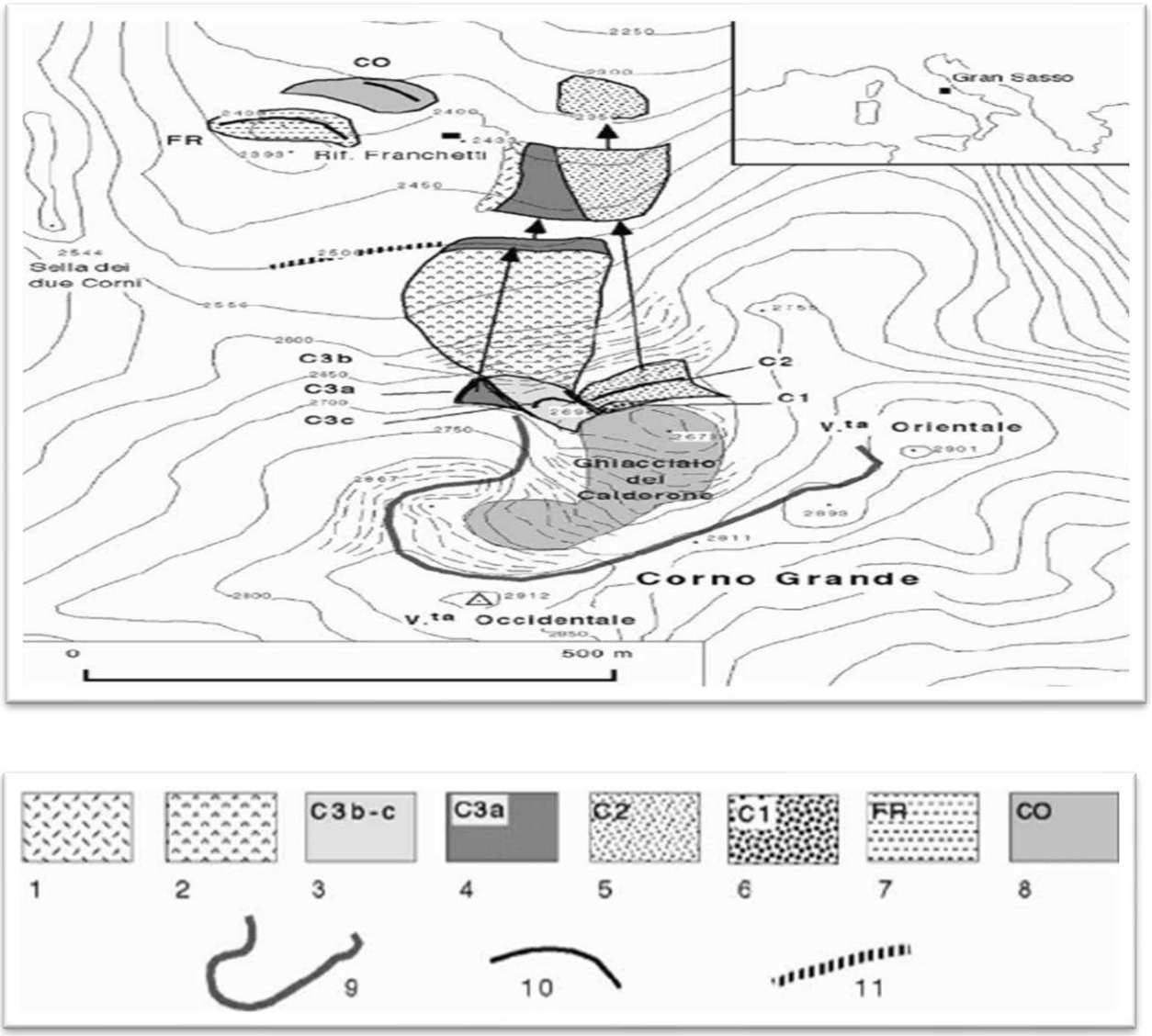

***Figure 9**: Geological sketch map of the studied glacial and slope waste deposits near the Calderone Glacier (Corno Grande-Gran Sasso Massif). Legend: slope waste deposits; 2 - stage Calderone 3b glacial debris; 3 - stage Calderone 3b, c moraines; 4 - stage Calderone 3a moraine and apron of fallen glacial debris; 5 - stage Calderone 2 moraine and apron of fallen glacial debris; 6 - stage Calderone 1 moraines; 7 - stage Franchetti moraine; 8 - stage Cornacchie moraine; 9 - cirque of the Calderone Glacier; 10 - moraine ridge; 11 - protalus rampart* [14].

The Calderone Glacieret, marked by yellow in Fig. 8, stands at an elevation range between 2650 to 2850 meters above sea level (a.s.l.). It is a small debris-covered glacier with the coordinates of 42°28’ N, 13°33’ E.

***Figure 10**: The Calderone Glacieret.*

The formation history of the Gran Sasso (The Corno Grande)

The formation of the Gran Sasso massif can be traced back to the Mesozoic era, which lasted from around 252 to 66 million years ago. During this time, the region that would eventually become the Apennines was submerged under a shallow sea. The accumulation of sediments, including marine organisms like shells and coral reefs, led to the formation of layers of sedimentary rocks, particularly limestone.

The Apennine region, including the Gran Sasso area, experienced tectonic activity during the Alpine orogeny, a series of mountain-building events that began around 65 million years ago and continued for millions of years. These tectonic forces were primarily caused by the collision of the African and Eurasian tectonic plates. This collision resulted in the uplifting and folding of the Earth's crust, leading to the formation of mountain ranges, including the Apennines.

Over time, the Apennines, including the Gran Sasso massif, continued to experience uplift and erosion. Glacial activity during the Pleistocene epoch, which began around 2.6 million years ago, played a significant role in shaping the landscape. Glaciers carved out U-shaped valleys and cirques, leaving behind the characteristic features seen today.

The specific geological processes and timeline for the formation of the Gran Sasso massif would involve detailed studies of rock formations, fossils, and tectonic movements in the region.

However, in broad terms, the massif's formation is the result of sedimentation, tectonic forces, and erosion over millions of years.

Geophysical investigation in Apennines (The Calderone Glacieret.)

The study conducted by PECCI M., DE SISTI G., MARINO A. & SMIRAGLIA C. in 2001, with the use of the GPR methodology, evaluated the maximum ice thickness to be approximately 27 m [18]. Another study by Monaco and Scozzafava in 2015 (using GPR again) showed an evident reduction in the maximum thickness to 26m [15].

Our investigations were carried out in March 2022, with the help of GPR and FDEM techniques. The goal was to determine the maximum thickness of the ice-rich layer and update our models that were built upon previous studies. The ice-core samples from the Calderone will be held in the "Ice Memory" World Archive in Antarctica [16].

In Calderone Mountain, two acquisition lines were investigated:

- Line 1 (green line in Figure 11) stretches along the glacieret development. (135m)
- Line 2 (red line in Figure 11), orthogonal to the direction of the glacieret development. (85m long).

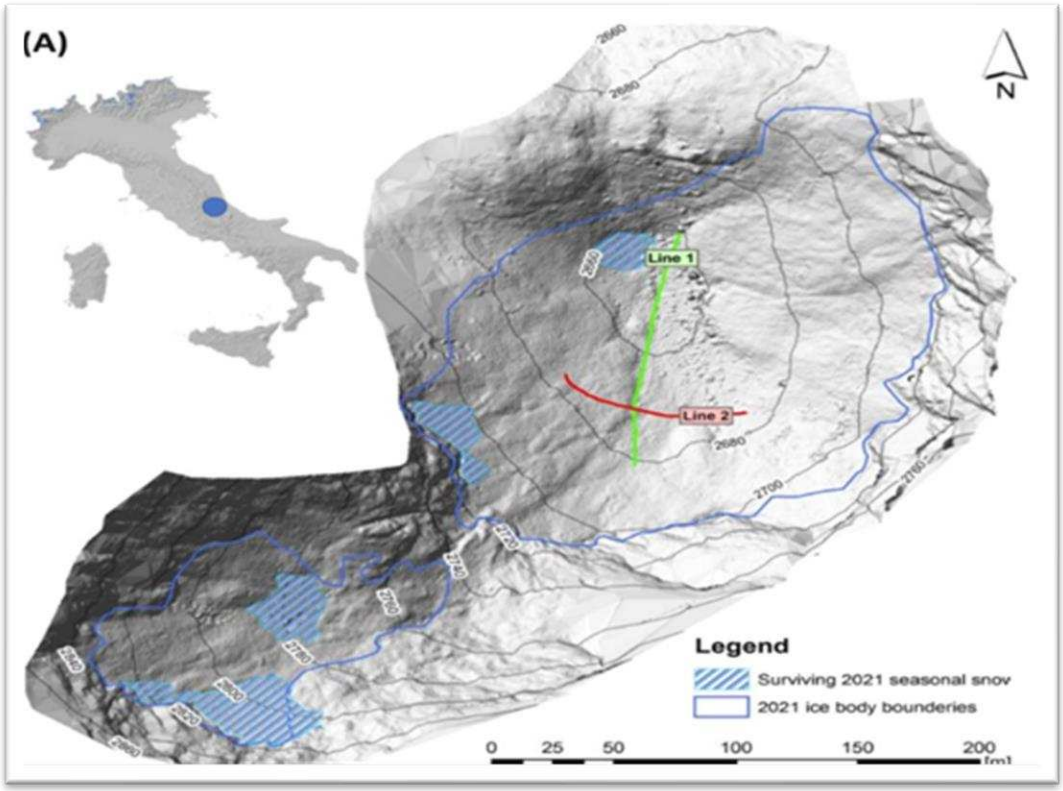

***Figure 11**: Calderon investigation lines. Line 2 is in red and line 1 is in green.*

First of all, we are going to define Rock glaciers and Permafrost.

Rock glaciers

A rock glacier consists of coarse rock fragments known as talus embedded in an ice matrix. This unique formation gradually accumulates and moves downslope, driven by the force of gravity. While sharing some similarities with traditional ice glaciers, rock glaciers exhibit distinct characteristics and behaviors.

Unlike active glaciers that composed primarily of ice, rock glaciers require the interplay of both talus and ice for their growth and movement. These rugged formations thrive in mountainous regions abundant in talus deposits. The continental settings with low precipitation and mean annual temperatures around 0°C is particularly suitable for their development. The movement of rock glaciers is governed by gravity, as the ice within them relies on permafrost. Whether formed by glacial or periglacial processes, the depth of the ice within rock glaciers must be sufficient to remain unaffected by the seasonal thawing of the active layer of permafrost, a result of periglacial processes driven by freezing cycles.

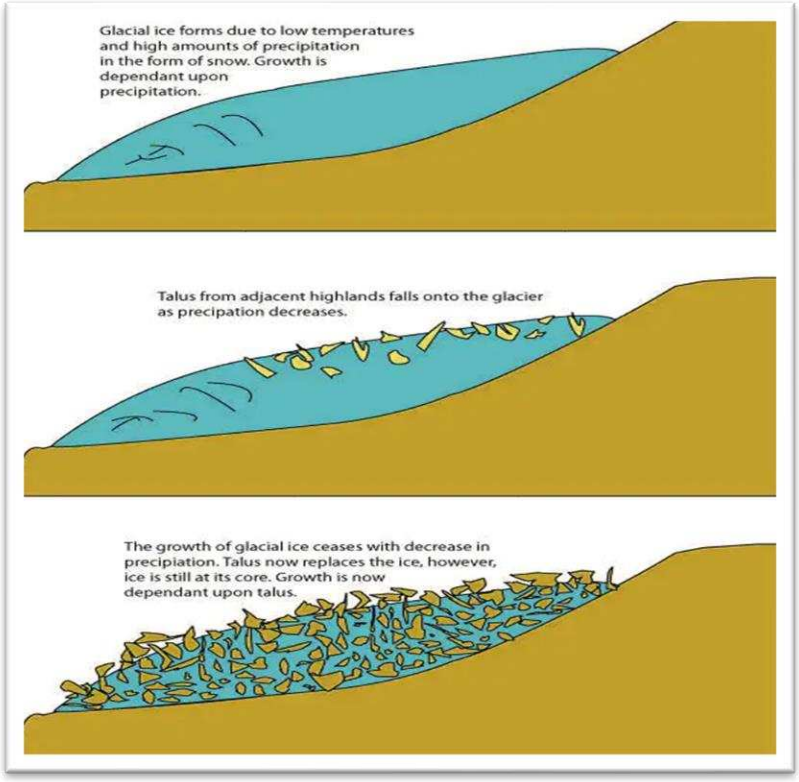

Figure 12) The rock glacier formation. The ice effectively cements the glacier together with talus on top. [17]

Rock glaciers can be classified into different types: Glacial, Periglacial and Tongue-Shaped and Lobate rock glaciers.

Glacial rock glaciers were once active glaciers that experienced ablation—a process involving the gradual melting of ice over time. This resulted in the ice's decay being substituted with the influx of talus and rock fragments from the nearby highlands. Ablation, brought on by melting, leads to the glacier's dependence on precipitation declining while temperatures remain around 0°C. What was once sustained by precipitation transitions to relying on talus, causing the glacier to transform into a rock glacier.

Periglacial rock glaciers arise from periglacial processes and consist of talus fields sourced from adjacent highlands. Intense freezing (frost) and snowmelt contribute to the accumulation of ice at the core of the rock glacier, as talus accumulates atop it. Both types of rock glaciers may seem physically identical, but their distinction lies in the analysis of the region's glacial history or the mapping of periglacial features to gauge the extent of Pleistocene glaciation, if any.

Tongue-shaped rock glaciers boast greater length than width and typically find their place within narrow valleys or cirques. Talus is derived from steep, rocky highlands near the glacier's origin point. On the other hand, lobate rock glaciers exhibit greater width than length, with talus originating from the enclosing valley walls that encompass the lobate rock glacier. Talus contributes to the growth of lobate rock glaciers from multiple sides, while in tongue-shaped rock glaciers, it only contributes to growth at the glacier's head. (Refer to figure 12)

Rock glaciers can be classified into three primary types based on their current conditions: active, inactive, and fossil rock glaciers forms.

Active rock glaciers stand out with their deforming ice and well-defined ridges, formed by the continuous downslope movement of the rock glacier. Evident by their steep frontal slope, analogous to a terminal moraine on traditional glaciers, active rock glaciers display ongoing dynamic behavior. In contrast, inactive rock glaciers share many characteristics with their active counterparts, except for their lack of movement downslope. The most noticeable distinction lies in the gentler frontal slope of inactive rock glaciers. Lastly, fossil rock glaciers differ from the others as they lack any ice content and exhibit no movement. Distinguished by the presence of vegetation and shaped by natural weathering processes, fossil rock glaciers have undergone significant geomorphic changes over time.[17]

Therefore, rock glaciers can be covered by a layer of rock debris, or it can be predominantly composed of rock with interspersed ice. Unlike ice glaciers, which often have visible ice surfaces, rock glaciers usually have minimal visible ice at their exterior. This can make them appear more like rocky slopes rather than traditional glaciers, especially when viewed from a short distance.

Rock glaciers exhibit slow movement, typically ranging from a few centimeters to a few meters per year. This slow pace of movement is one reason why their glacial nature might not be immediately apparent. The movement usually originates in the ice located in the lower sections of the rock glacier. The surface rocks then adjust to this movement, occasionally forming distinctive features like ridges or flow patterns.

The growth of a rock glacier involves the accumulation of ice and rock debris. The ice mass grows through precipitation, local runoff, spring discharge, and contributions from avalanches. The rock mass accumulates through talus deposits from the cirque head and valley walls, as well as from

landslides. The heat of the sun melts snow and ice on the surface, causing meltwater to seep downward into the glacier and freeze, carrying mud and fine rock debris along with it. However, the upper portions of a rock glacier experience lose ice, snow, and water through processes like ablation, melting, runoff, and evaporation.

In terms of the Size and Scale, Rock glaciers are generally smaller than traditional ice glaciers. A larger rock glacier might be around fifty meters thick and a few kilometers in length. The size and appearance of the surface rocks can vary based on their source and supply.[17]

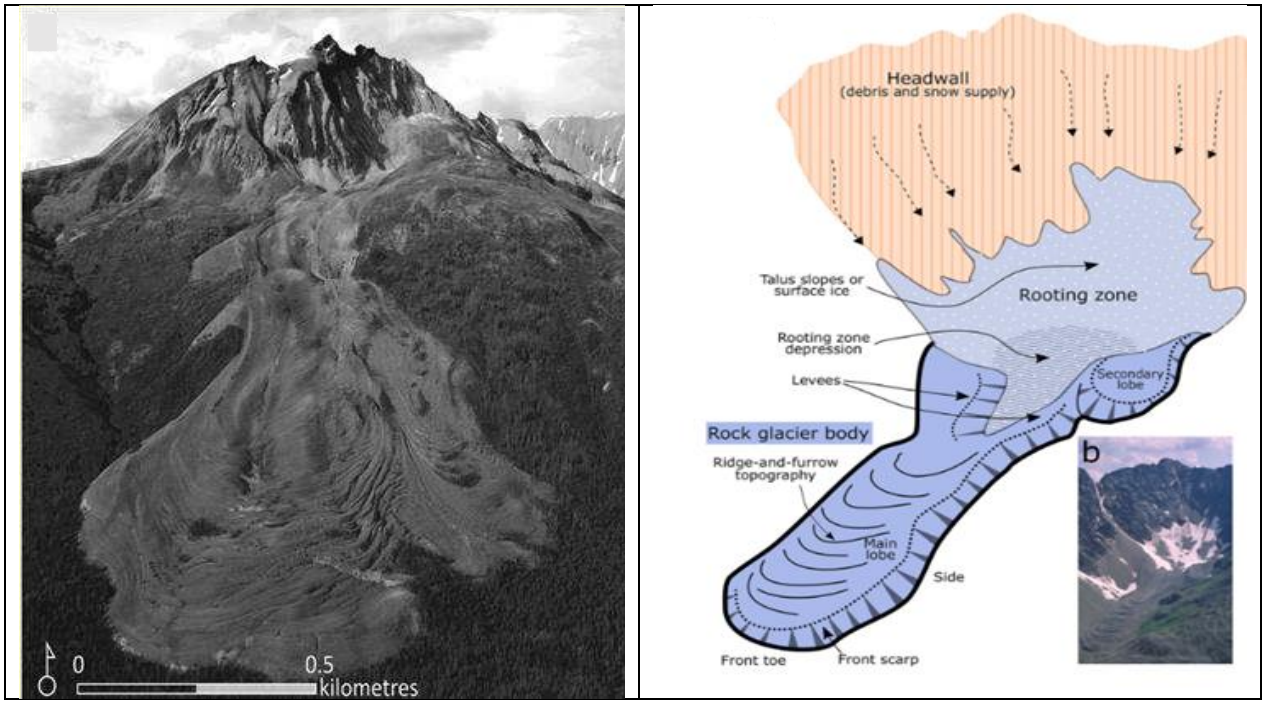

***Figure 13**: The main morphological components of a typical tongue-shaped rock glacier and the corresponding field photograph. Buco del Cacciatore, Valtellina, Central Italian Alps (photo courtesy of Mario Butti, retrieved on wileyonlinelibrary.com).*

Permafrost refers to a permanently frozen layer of soil, sediment, and rock that remains below the freezing point of water (0°C or 32°F) for at least two consecutive years, often much longer. It is typically found in cold regions, such as polar and high-altitude environments, and extends to varying depths beneath the ground surface. Permafrost plays a crucial role in shaping landscapes, influencing vegetation patterns, and impacting infrastructure, as its thawing can lead to ground subsidence, land instability, and changes in hydrological conditions.

The active layer of permafrost is the uppermost layer which thaws during the summer and freezes again during the winter. It experiences seasonal temperature fluctuations and is usually a few meters thick. The colder the climate, the thinner the active layer. Therefore, thin active layers can be found in the high arctic, whereas the thickest active layers occur near the southern limits of permafrost. The thickening of the active layer results in the melting of internal ice within the rock glacier. This ice serves as a stabilizing agent, holding the debris together. As a consequence, the mechanical stability of the rock glacier diminishes, making the debris more prone to erosion. This ultimately increases the amount of erodible material which can lead to landslide and Ground Instability.

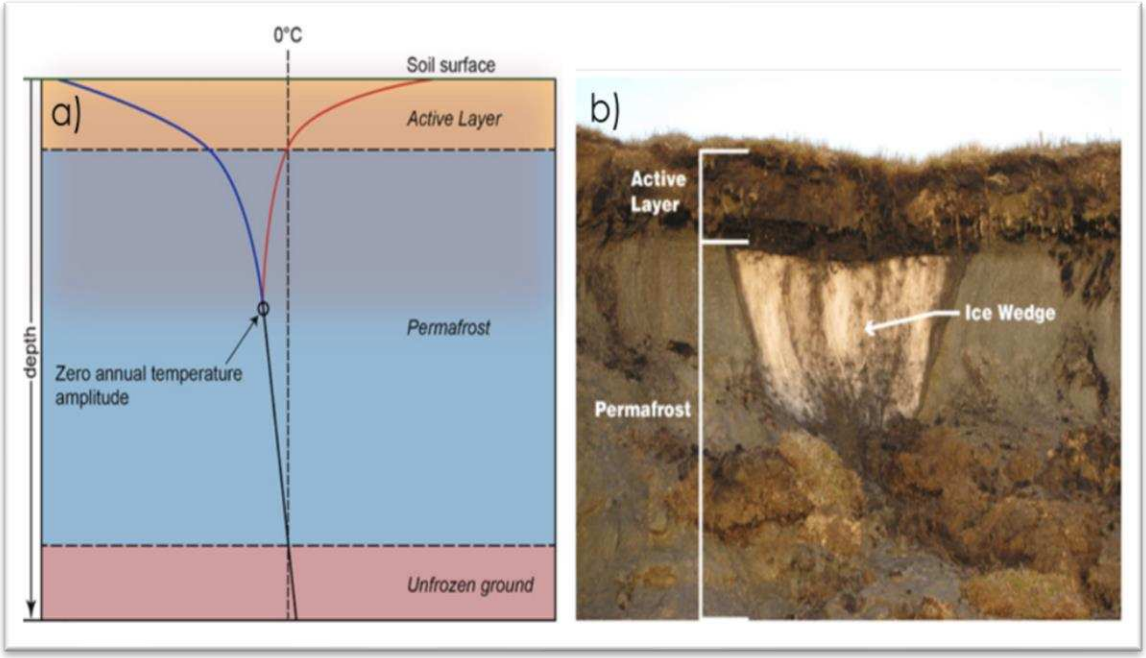

***Figure 14**: Climate-Driven Impacts on Permafrost (Processes and Effects of Temperature Changes and Snow Cover Dynamics). Photo credit: Benjamin Jones, USGS, Public Domain (Modified by NASA)*

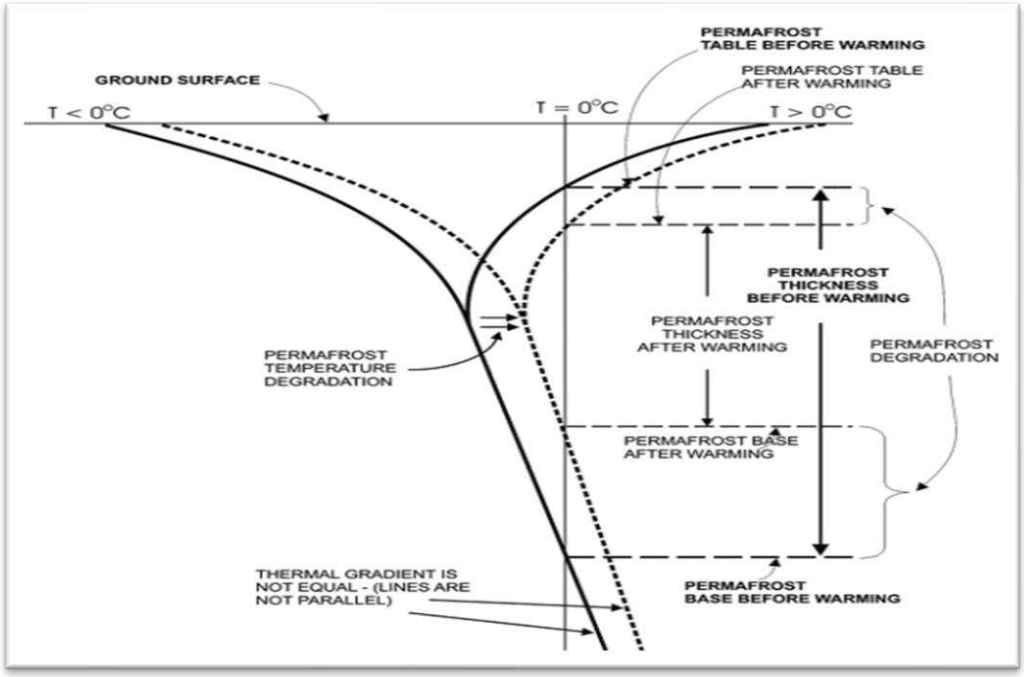

***Figure 15**: Potential permafrost degradation processes depicted in the illustration from Dobinski's 2011 study* [18].

Temperature fluctuations will primarily impact permafrost through the processes highlighted in Figure 15. These processes include (a) thickening of the active layer, (b) elevation of permafrost temperature, (c) reduction in permafrost thickness, and (d) decline in ice content.

The initial negative impact of climate warming is the increase in the active layer thickness. This change is closely tied to year-to-year variations, shaped by the previous winter's thermal state and summer temperatures.

Rock glaciers often exhibit a significant contrast between the rough, chunky active layer and the underlying permafrost. The permafrost layer is more solid and rigid than the active layer. Therefore, they react differently to changes in temperature. The active layer can thaw and freeze seasonally, causing it to become loose and move. But the frozen layer below stays solid and doesn't change as much. The increase in the active layer is associated with the loss of ice at the permafrost table and a lowering of the terrain.

When permafrost thaw penetrates beyond the typical seasonal frost depth, the entirety of the thawed layer might not fully refreeze during winter. This results in a persistently unfrozen layer, known as a "Talik," between the periodically frozen surface layer and the deeper permafrost. Such occurrences arise when the permafrost warms and loses its surface cooling. This could be a transitional phase after an unusually warm year or a permanent change due to permafrost inactivation. These shifts are expected in the future at the lower bounds of discontinuous permafrost regions.

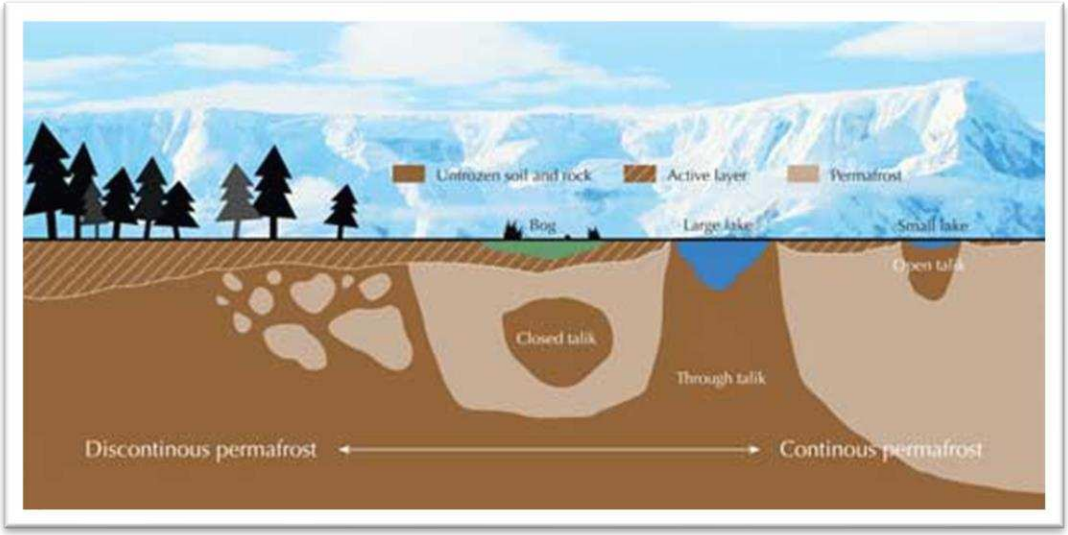

Figure 16.Modified image courtesy of PhysicalGeography.net; background image courtesy of Mark Sykes; image source: Flickr

Permafrost warming occurs slowly due to the ground's low thermal conductivity, particularly in ice-rich permafrost, this heat transfer takes years to propagate through the profile. Consequently, the permafrost temperature is more responsive to decade-long trends than to short-term fluctuations.

Heat waves propagating downward through the profile can be deduced from certain borehole profiles, where the lowest temperature is recorded at greater depths compared to the zero annual amplitude (ZAA). Over time, reduced surface cooling allows for bottom-up warming due to the geothermal heat flux.

The snow cover plays a crucial role in these developments. While one might expect a linear relationship between ground temperature and air temperature, ground surface temperature monitoring reveals a more complex connection. The insulation capacity of the snow cover induces significant deviations from air temperature trends.

The commencement and thickness of the snow cover during early winter carry significant weight. November to January sees the shortest days and minimal direct radiation, even as air temperatures drop considerably. In the absence of snow cover, the soil experiences a sharp cooling. A shallow snow cover could even amplify heat loss. Conversely, an early and thick snow cover prevents soil cooling and retains the accumulated heat from the prior summer and autumn.

Snow cover history during early winters largely dictates winter ground surface temperature and the winter equilibrium temperature (WEqT), representing the average ground surface temperature in February and March. For areas with seasonal frost, it determines soil freezing state, as well as frost depth.

Snow cover thickness during winter has a significant importance. A substantial cover (at least around 0.8-1 meter) insulates the ground from air temperature shifts and maintains the thermal state acquired during the fall and early winter. A shallow or discontinuous present snow cover (due to wind deflation) allows ongoing ground cooling throughout winter.

In spring, snow cover duration exerts an opposite effect compared to early winter. Delayed snow melt, shields the soil from direct solar radiation during a period of maximum exposure, insulating it from sensible heat flux. Conversely, early snow melt accelerates soil warming. Thus, the winter cooling impact of a shallow snow cover can be mitigated by an early snowmelt.

Snow Cover has a huge Influence on temperature variability. It can act as a blanket or insulator on the ground, can affect how temperatures change from year to year. Sometimes, the presence of snow can cause the actual temperature to be different from what the atmosphere's temperature. for instance, during relatively mild winters, the presence of snow can make it feel even colder than expected. Conversely, in colder winters, the snow cover might create a sensation of warmth. However, we're unsure about the long-term effects of snow cover on temperature trends over many years. Borehole temperature records, which measure temperature changes in deep holes, reveal that there was a warming trend from 1987 to 1994. After that, temperatures stabilized, which contrasts with what was happening on the surface, where it might have seemed like cooling was occurring. This highlights the complex relationship between snow cover, surface temperatures, and deeper temperature trends.[19]

Therefore, the thermal evolution of permafrost and ground temperatures depends on both air temperature and the presence of snow cover. Most climate models predict growth in winter precipitation, which, it materializes as snowfall, could yield diverse effects, according to its season:

- Early snowfalls could intensify the warming.

- A robust winter snow cover would similarly contribute to warming.

- A delayed snowmelt would hinder the warming of the ground.

However, these snow cover effects are relevant mainly in regions with moderate slopes where substantial snow cover can develop and persist throughout winter. In contrast, steep rock faces remain unaffected by snow cover.

Glacieret

A glacieret, a smaller version of a glacier, shares a similar movement to larger glaciers, although at a slower pace and over a smaller expanse. Just like their larger counterparts, glacierets respond to gravity, causing them to slide gradually downward. However, due to their compact size, the movement of glacierets is less noticeable and proceeds more gradually.

The movement of glacierets is influenced by factors such as the steepness of the terrain, the thickness of the ice, and the presence of water beneath, which assists in reducing friction. Although the movement of glacierets might not be as visually dynamic as larger glaciers, its significance in shaping these ice-rich landscapes over time cannot be undermined.

In addition to their movement, glacierets share other features with glaciers, including the presence of crevasses (cracks in the ice), distinct areas where snow accumulates and where ice melts (accumulation and ablation zones), and a responsiveness to shifts in the climate. Despite their smaller size, glacierets play a crucial role in the understanding of climate change and transformations in these frozen environments. Considering this, we can recognize the significance of our research, which contributes to our understanding of these important but often underestimated features of our natural environment.

The dynamics of the glaciers

Glaciers, characterized as mobile masses of ice, originate through the compaction and recrystallization of snow in frigid locales. The evolution of a glacier spans from decades to millennia, its dimensions depend upon the volume of ice accumulated over its lifespan. Annually, glaciers undergo fluctuations in mass, accumulating snow and precipitation in their upper reaches (accumulation zone), while experiencing mass loss in their lower portions (ablation zone) due to partial melting, particularly during the warmer months. In instances of marine-terminating glaciers, an additional source of mass loss arises from the calving of icebergs that detach and drift away.

The equilibrium between accumulation and ablation delineates the glacier's mass balance. When accumulation surpasses ablation, the glacier achieves a positive mass balance, resulting in advancement. Conversely, if ablation surpasses accumulation, the glacier exhibits a negative mass balance, prompting retreat (see Figure 17). The glacier's terminus position signifies its endpoint at any given juncture. Fluctuations in the terminus point serve as a crucial metric for tracking long-term dynamic glacier behaviors. Alterations in the rate of terminus movement are dependent upon

shifts in glacier dynamics. For instance, heightened accumulation can accelerate glacier velocity, culminating in frontal progression. [20].

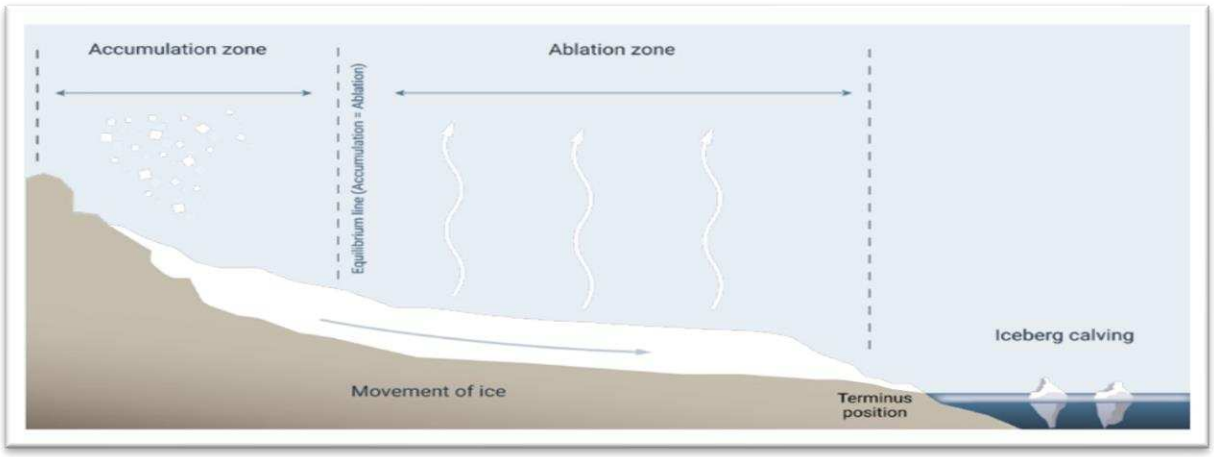

***Figure 17**: Simplified diagram of glacier dynamics, image from UNESCO* [20].

History of Glaciers in the Alps and Apennines

The formation of glaciers in the Alps traces back to the Pleistocene era, often referred to as the "Ice Age," which began around 2.6 million years ago. During this time, Earth experienced a series of glacial and interglacial cycles, characterized by fluctuations in global temperatures. As temperatures dropped, snowfall accumulated in the high-altitude regions of the Alps, gradually transforming into ice under immense pressure.[21]

Over the millennia, glaciers in the Alps advanced and retreated multiple times in response to climatic shifts. During glacial advances, these massive ice masses spread out, shaping valleys, and carving out U-shaped troughs through the mountains. Conversely, during periods of warming temperatures, glacial retreats left behind a series of traces, such as moraines and glacial erratics, providing evidence of their former presence. In other words, Glaciers played a pivotal role in creating the unique Alpine topography we see today.

While there are glaciers in the Alps, located further North, the Apennines have a milder climate, and glaciers are less prominent in this region. Throughout history, the Apennines have been essential in shaping the geographical landscape of Italy.

At the beginning of the third millennium, there were only a few small glaciers in southern Europe. after the Corral de la Veleta Glacier vanished in 1913 in the Sierra Nevada region of Spain, the Calderone Glacier became the southernmost glacier in Europe [22].

During the 20th century, the glacier underwent a significant retreat. Research indicates that between 1916 and 1990, its volume decreased by approximately 90%, while its area reduced by about 68% [23].

In 2009 Ghiacciaio del Calderone was divided into two small glacier patches (glacierets). Glaciers are not present elsewhere in the Italian Apennines. These alarming figures raise concerns about the

future condition of Calderone's glaciers. If current trends continue, Calderone Glacier could experience a similar fate as Corral de la Veleta Glacier [22].

In the following image (fig. 18), The Calderone Glacier is depicted on this aerial map. The light blue dotted line illustrates the surface extension of the ice body during the 19th century, whereas the two light blue areas indicate the current extension of the two ice aprons [24].

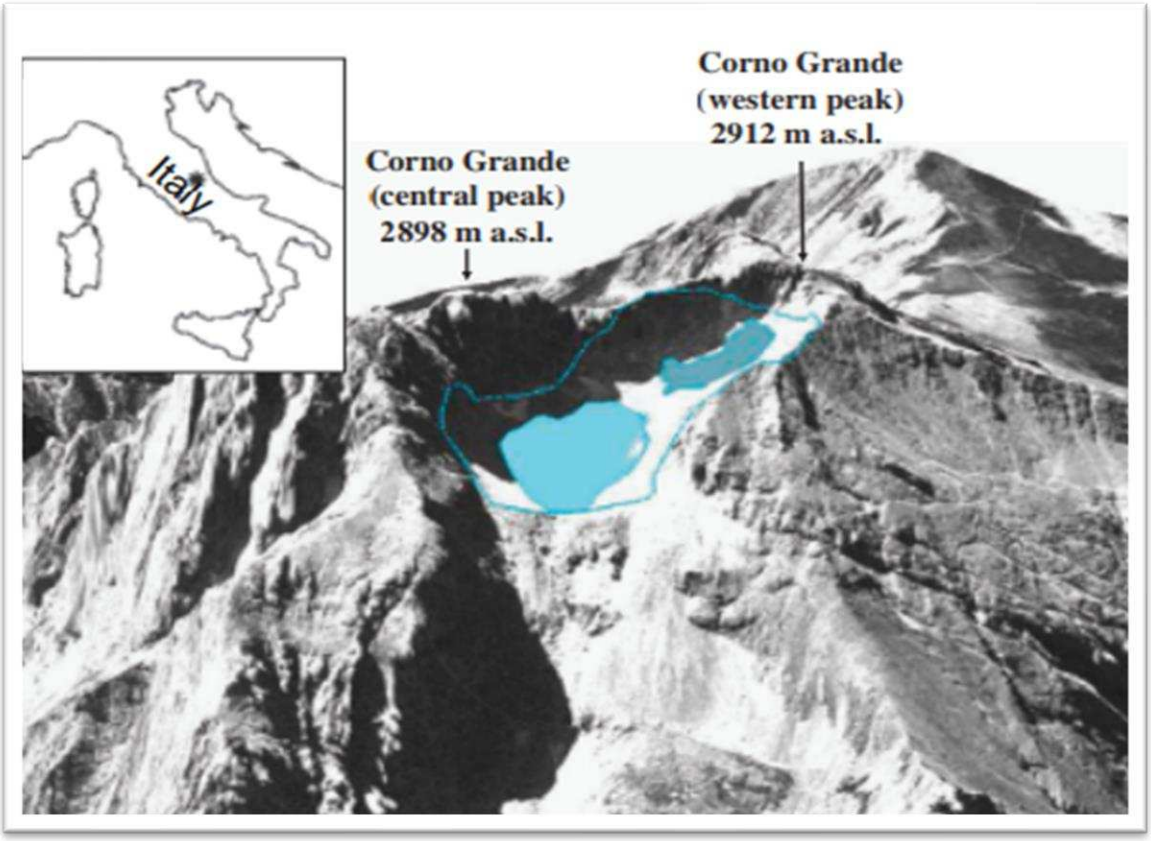

***Figure 18**: Aerial map of the Calderone Glacier* [24].

Methodology

In this section, we will explore the theoretical principles that govern the electromagnetic induction method technique, as well as a brief overview of the GPR and ERT methods. Finally, an in-depth description of the instrumentation and equipment deployed for data acquisition will be presented.

Electrical resistivity tomography (ERT) method

The Electrical resistivity technique is a long-established, traditional geophysical method of investigation. That is currently one of the most popular and frequently used instruments for civil engineering and environmental prospecting [25].

The electrical survey aims to determine the subsurface resistivity distribution, carrying out measurements on the ground surface or inside the borehole called Resistivity logging by suspending electrodes in boreholes. With the use of this technique, it is possible to reach a high resolution close to the electrodes for deeper investigations.

This method is sensitive to the contact between soil and electrodes, so-called “Galvanic contact.” In some cases, this problem can be solved by adding conductive gel or salt water around the electrodes, which can reduce the contact resistance between the electrodes and the soil, improving the signal-to-noise ratio.

Regarding our study area, ERT is a popular and the most used method for permafrost and rock glacier studies. This is because of its high accuracy and effectiveness.

Electrical prospecting is a valuable approach to studying frozen alpine subsoil because it can distinguish frozen and non-frozen debris according to their resistivity differences. It can be used to determine the active layer thickness (ALT) of the permafrost giving information about the changes in the ice/water ratio over time [5].

Due to the snow cover acting as an electrical insulator, this survey is usually not possible in winter or when a thick layer of ice is covering the surface.

Basic Principles of the method

In the resistivity method, the apparent resistivity, ρa (Ωm), is determined with the help of two (current) electrodes that inject the current into the ground and another pair of electrodes that measure the potential difference (voltage) [26].

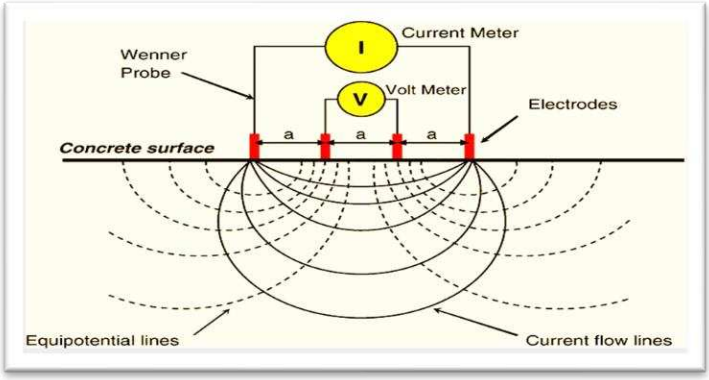

***Figure 19**: The voltage V between two electrodes is measured after a direct current I is injected through a pair of electrodes* [27].

The basic principle of the electrical resistivity method is based on Ohm's law:

$$\Delta V = I R$$

It describes the relationship between current flow (I), potential difference voltage (V), and resistance (R).

Calculating the apparent resistivity (ρa) of the medium is possible by knowing the geometrical configuration of the electrodes, the current intensity (I), and the potential difference (V) using the following formula:

$$\rho a = k \, \Delta v / I$$

The K here is called "the geometric factor, which depends on the configuration of current and potential electrodes (Wenner, Schlumberger, Dipole-Dipole, and so on) and the surface geometry. When the topography is complex, k is unknown, so it can only be determined numerically.

Generally, the electrical resistance is transformed into apparent resistivity by using the geometric factor k.

Generalized formula for calculating K for a four-electrode configuration is:

$$K = 2\pi\,(1/C1P1 - 1/C1P2 - 1/C2P1 + 1/C2P2) - 1.$$

In a homogeneous medium, the apparent resistivity is the same as the true resistivity.

For non-homogeneous distributions, however, these values are not equal. In order to estimate the true resistivity from the apparent resistivity, inversion is required to estimate the most accurate model of the subsurface [21].

For two-dimensional (2D) ERT, in order to have a pseudo-section of apparent resistivities the measurements should be conducted across the whole electrode array [24].

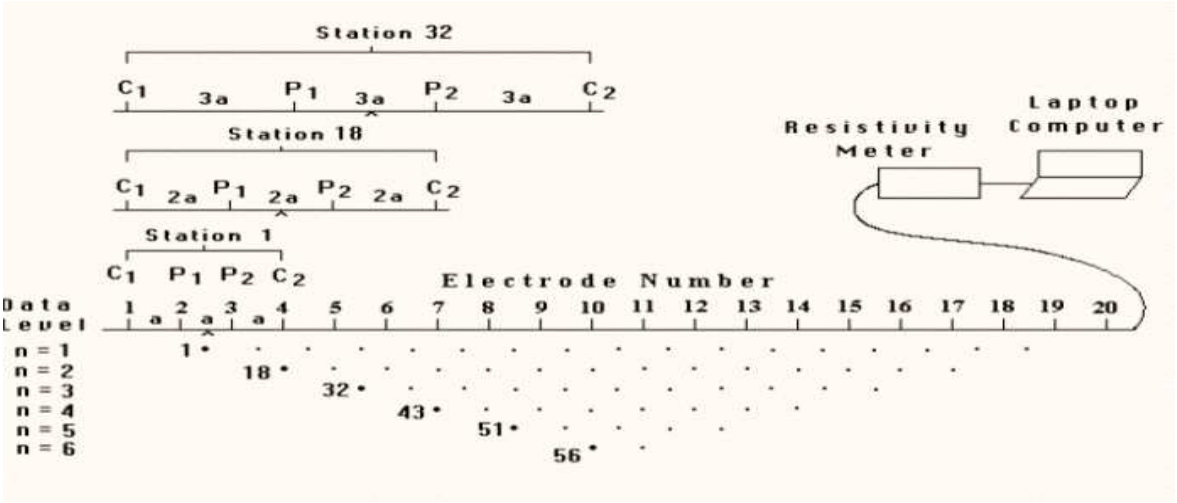

***Figure 20**: 2-D electrical survey (ERT) Wenner array, pseudo section [21].*

Influential factors and Electrodes configuration

There are numerous factors that affect ground resistivity, such as moisture content, porosity, degree of cementing, degree of saturation, the soil or rock texture, and so on [28].

Furthermore, the depth of the investigation will vary based on the electrode spacing. In other words, increasing the distance between the two current electrodes allows the current to penetrate deeper into the subsurface. Moreover, the resolution is higher closer to the electrodes. Consequently, the distance between the electrodes is a crucial acquisition factor.

There are several different electrode array combinations widely used for multi-channel resistivity measurements, such as the Schlumberger, Dipole-Dipole, and Wenner array, and a combination of them.

The Werner array consists of current electrodes at both ends and voltage electrodes in the middle. There is equal spacing between all electrodes. This method provides an excellent vertical resolution.

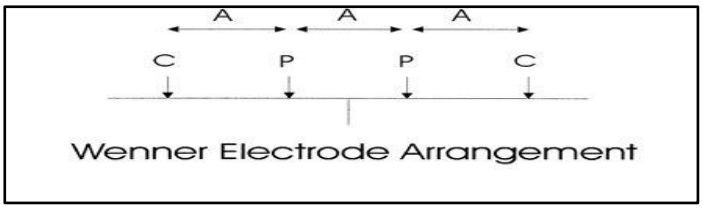

***Figure 21**: Wenner array* [29].

The Schlumberger configuration is similar to Wenner's. The only difference is that the spacing between current and potential electrodes is n times the spacing between potential electrodes.

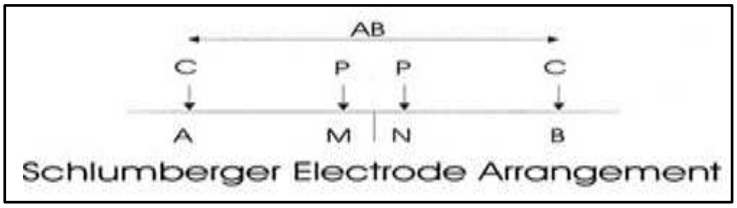

***Figure 22**: Schlumberger array* [29].

The Dipole-Dipole array consists of current electrodes on one side and potential electrodes on the other, as shown in the figure below. This method is highly sensitive to lateral changes in subsurface resistivity, making it suitable for detecting and imaging horizontal features such as geologic layers or boundaries. This is due to the fact that the largest sensitivity values are located between the current electrodes (A, B) as well as between de potential electrodes (M, N). however, it may not be as effective at resolving vertical variations in resistivity.

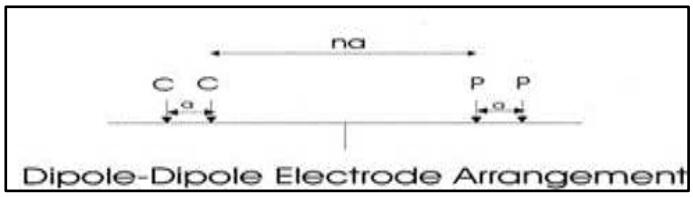

***Figure 23**: Dipole-Dipole array* [29].

In summary, Wenner and Schlumberger are better in-depth imaging, while Dipole-Dipole more suitable for imaging horizontal features.

Electromagnetic method (EM) Basics

Electromagnetic (EM) methods are geophysical techniques used to investigate subsurface structures and properties by measuring the response of materials to the application of electromagnetic fields. These methods rely on the principles of electromagnetism to obtain information about the distribution of electrical properties in the Earth's subsurface, Using a source antenna (Tx) and a receiver antenna (Rx) [23]. Different electromagnetic methods utilize various ways of generating and measuring electromagnetic fields. These methods can be categorized based on the electrical conductivity and the frequency of the applied electromagnetic fields:

- High Electrical Conductivity, Low-Frequency (EM induction methods),
- Low Electrical Conductivity, High-Frequency methods.

The following are the two main approaches to generating low-frequency EM fields:

1) The time-domain electromagnetic method (TDEM): This transient EM field is created by the abrupt switch-off of the current in a transmitter coil placed on the ground surface. The transient response is measured by a receiver coil during cut-off. The depth of investigation increases with the time during which the secondary field is measured after the primary field has been cut off.

2) The frequency-domain electromagnetic method (FDEM) transmits signals at a specific range of frequencies and detects changes in the amplitude and phase of the resultant field. EM surveys can be carried out using aircraft, ground-based, or down boreholes [25].

As previously stated, our focus will be directed towards the FDEM method.

Low-frequency EM methods are fast and easy to operate because, unlike resistivity techniques, they are independent of the nature of the ground. No direct (galvanic) contact with the ground is needed. This is a great advantage in high mountain environments, as getting sufficient electrical current into the ground is one of the largest problems in DC resistivity surveys. Furthermore, DC resistivity surveys in wintertime are usually impossible to conduct, as the snow cover acts as an electrical insulator [30] [31].

To further categorize induction EM methods based on their energy source:

The secondary fields may be excited by an artificial controllable source that is part of the EM instrumentation known as the active EM method [31]. That itself is divided into near field and far field, which will be discussed more in the EM principles section.

Another case is when the secondary fields are generated from a natural source, such as the natural Earth electromagnetic field (magnetotellurics or MT), which is referred to as a passive EM method [31].

EM Method's principle

Faraday's law states that whenever there is a change in the magnetic flux in a closed loop, an electromotive force is induced in that loop [32]

$$\epsilon.m.f = -\mathrm{N}.\left(\frac{\Delta\Phi\mathrm{B}}{\Delta\mathrm{t}}\right)$$

the induced emf is measured in Volts.

With the use of Faraday's law, we will be able to explain how the rotational electric fields in the surrounding area are induced by time-varying magnetic fields.

Based on Biot-Savart's law, magnetic fields are created by current density. Thus, currents induced by the primary field will create a secondary magnetic field that can be measured on the surface [31].

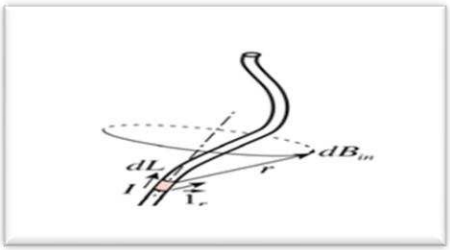

***Figure 24**: Bio-savart law.*

The magnetic field $\vec{B}$ due to an element $\vec{dl}$ of a current-carrying wire is given by:

$$\vec{B} = \frac{\mu_0}{4\pi}\int_{wire}\frac{I\overrightarrow{d\boldsymbol{l}}\times\hat{\boldsymbol{r}}}{r^2}$$

As a result of the variation in the induced electromagnetic field, the current measured at the receiving coil is the vector summation of both the primary and secondary "eddy" currents.

Maxwell's Equations:

Maxwell's equations are the fundamental equations that explain quantitatively electric and magnetic field propagation relationships in the air, ground, and even vacuum [33]:

***Table 1**: Maxwell Equations*

I. Gauss' law for electricity	$\nabla \cdot E = \frac{\rho}{\epsilon_0}$	In the absence of electric charges, the equation is equal to zero.
II. Gauss' law for magnetism	$\nabla \cdot B = 0$	Maxwell considered that there are no free magnetic poles.
III. Faraday's law of induction	$\nabla \times E = \frac{-\partial B}{\partial t}$	Changing the magnetic field in time produces an electric field.
IV. Ampere's law	$\nabla \times H = J + \frac{\partial D}{\partial t}$	Changing the electric field in time produces a magnetic field.

***Table 2**: Electromagnetic Quantities and Units*

Symbols definitions:		
E = Electric field [V/m]	ρ = charge density [C/m^3]	I = electric current [A]
B = Magnetic field [T]	ε_0 = free space permittivity $\varepsilon_0 = 8.85 \times 10^{-12}$ [F/m] ε_r= relative permittivity	J = current density [A/m^2]
μ0 = permeability of the free space μ0= 4π × 10^{-7} [H/m]	D = Electric displacement field [C/m²]	c = speed of light ($\frac{1}{\sqrt{\mu_0 \varepsilon_0}}$), [m/$s^2$]
H = Magnetic field strength [A/m]	M = Magnetization vector [A/m^2]	P = Polarization vector [C/m^2]
ω = angular frequency [Rad/s]	σ= conductivity [S/m]	μ_r= relative permeability

Constitutive equations in electromagnetism:

A general description of the relationship between the four field quantities is as follows:

$$\mathbf{D = D\ (E, H)}$$

$$\mathbf{B = B\ (E, H)}$$

In vacuum, the constitutive relations are defined as:

$$\mathbf{D} = \varepsilon_0 \mathbf{E}$$

$$\mathbf{B} = \mu_0 \mathbf{H}$$

However, for non-vacuum Isotropic homogeneous media, D and E, respectively, depending on the relative permittivity and relative permeability:

$$\mathbf{D = \varepsilon\ E,\ (\varepsilon = \varepsilon_0\ \varepsilon_r)},$$

$$\mathbf{B = \mu\ H,\ (\mu = \mu_r\ \mu_0)},$$

A material becomes polarized or magnetized when exposed to an external electric or magnetic field. As a result, the electric flux density in a medium can be expressed as:

$$\mathbf{D} = \boldsymbol{\varepsilon_0 E} + \mathbf{P}$$

Similarly, the magnetic flux density in a magnetic medium can also be expressed as follows:

$$\mathbf{B} = \boldsymbol{\mu_0 H} + \boldsymbol{\mu_0 M}$$

In the case of a conducting medium and in the absence of a magnetic field: the current density and electric field relationship will be defined as:

$$\boldsymbol{J} = \sigma \boldsymbol{E}$$

All materials have magnetic properties and are affected by magnetic fields to some extent. And according to their magnetic behaviour, magnetic materials can be divided into three main categories:

1) Paramagnetic material
2) Diamagnetic material
3) Ferromagnetic material.

In a Paramagnetic material ($\mu_r > 1$), While there is no external magnetic field, dipole moments are oriented randomly, resulting in zero net macroscopic magnetization[34], [35].

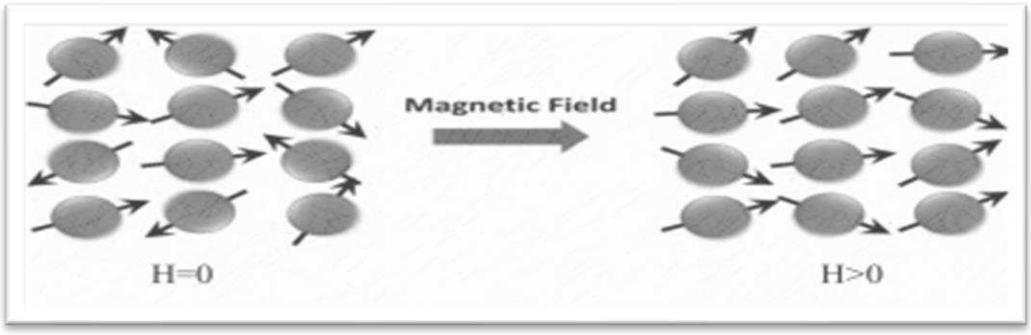

***Figure 25**: This figure illustrates the dipole configuration for a paramagnetic material both without and with an applied magnetic field (H)* [35].

Diamagnetic material ($\mu_r < 1$): in the absence of external magnetic field (*H*) it is assumed that there is no net magnetic moment.

In the presence of an external magnetic field instead, electrical current and thus a magnetization (*M*) will be produced in opposite direction with respect to our field [35].

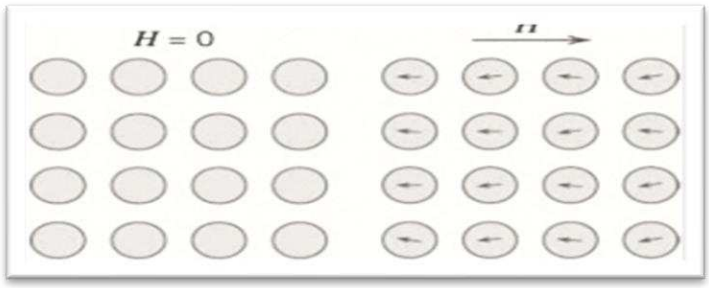

***Figure 26**: An illustration of magnetization of diamagnetic materials, with μ of less than that of vacuum* [35].

Ferromagnetic material ($\mu r \gg 1$):

In absence of an external magnetic field, this type of material has a spontaneous net magnetization. Conversely, in presence of an external magnetic field they will be strongly magnetized in the direction of the field. Ferromagnetic materials have very high permeabilities [33].

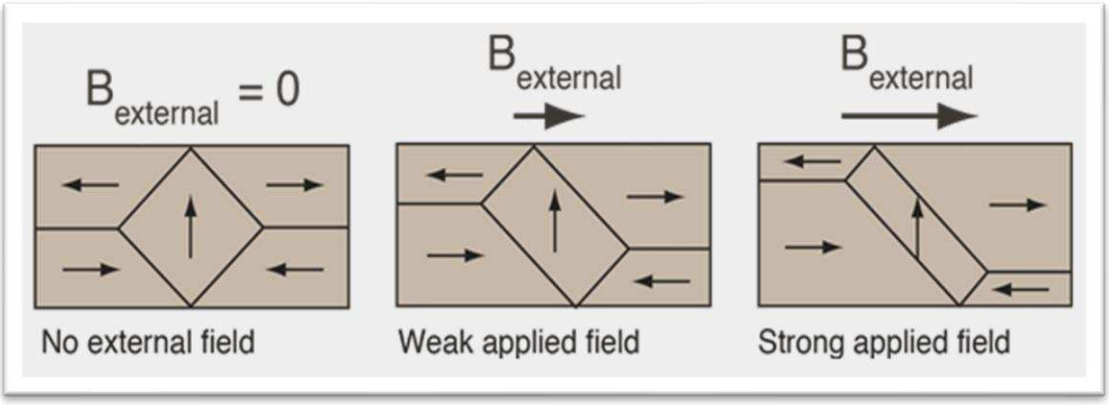

***Figure 27**: Ferromagnetic material in absence and in presence of an external magnetic field (B)* [35].

Finally, by combining Maxwell's equations with the constituent relationships (equation **III** and **IV**), it is possible to rewrite the EM field equations in the form of dissipative wave equations.

In a homogeneous medium:

For the magnetic field:

$$\nabla^2 \bar{H} - \sigma\mu \frac{\partial \bar{H}}{\partial t} = \varepsilon\mu \frac{\partial^2 \bar{H}}{\partial t^2}$$

For the electric field:

$$\nabla^2 \bar{E} - \sigma\mu \frac{\partial \bar{E}}{\partial t} = \varepsilon\mu \frac{\partial^2 \bar{E}}{\partial t^2}$$

When the signal frequency is lower than 100kHz, the second term of the equation is much smaller than the first, and the regime is called *inductive,* with the diffusion of fields.

As a result, for Conductor case; when $\sigma >> \omega\varepsilon$:

$$\nabla^2 \mathrm{E} = \mu\sigma\left(\frac{\partial E}{\partial t}\right)$$

When the signal frequency is higher than 10 MHz, the first term becomes negligible, and the propagation term becomes important.

As a result, for dielectric case; when $\sigma << \omega\varepsilon$:

$$\nabla^2 \mathrm{E} = \mu\sigma\left(\frac{\partial^2 E}{\partial t^2}\right)$$

By transferring the dissipative wave equation into the frequency (w) domain via Fourier transformation:

a) Wave equation for the electric field in the frequency domain:

$$\nabla^2 \mathbf{E} - j\mu\omega\sigma\mathbf{E} = \mu\varepsilon\omega^2\mathbf{E}$$

b) Wave equation for the magnetic field in the frequency domain:

$$\nabla^2 \boldsymbol{H} - j\mu\omega\sigma\boldsymbol{H} = \mu\varepsilon\omega^2\boldsymbol{H}$$

The LOSS FACTOR (P): by making the ratio between the attenuation term and the propagation term, the loss factor is obtained as follows:

$$P = \frac{\mu\omega\sigma}{\mu\varepsilon\omega^2} = \frac{\sigma}{\varepsilon\omega} = \frac{1}{\rho\varepsilon\omega}$$

When **P>>1**: we have a **diffusive field** which means high electrical conductivity and low frequency (EM induction).

As stated before, there are two EM induction methods available in diffusive conditions:

- FDEM, or frequency-domain electromagnetic method,
- TDEM, or time-domain electromagnetic method.

FDEM itself consists of two types:

a) Near field techniques: it is a low induction number method in which the source and receiver are close to each other. Therefore, the primary field does not undergo any phase shift.

b) Far-field techniques: plane-wave methods, where the source of the primary field is so far away that the produced field is considered uniform in the area of exploration.

When **P<<1**: we have a **wave propagation field** which means low electrical conductivity and high frequency. The available method in this range of frequency is the Geo-radar or GPR.

Ground penetrating radar (GPR)

It is a high-frequency EM technique (10-2500 MHz), that measures the Dielectric permittivity of the subsoil and due to its short wavelength offers a high-resolution image. Thus, it is mostly used just for shallow targets (higher frequencies provide better resolution but have reduced penetration depth).

GPR is mostly used to detect the presence of anomalies in the subsurface and are of two types:

- Monostatic: when emitter and receiver antennas are in the same probe.
- Bistatic: when the emitting antenna and receiving one are separated, which is useful to get the Radar wave transmission velocity and the depth of the subsurface targets.

GPR provides real-time results and can quickly cover large areas. It is particularly useful to study the subsurface characteristics of frozen environments such as permafrost and glaciers and to investigate the dynamics of glaciers as ice and snow exhibit low attenuation due to their dielectric properties (please refer to the table3).

Table 3: Attenuation, Resistivity, and Relative Permeability of Materials

Material	Attenuation α (dB/m)	Resisitivity ρ (ohm/m)	Relative permittivity ε_r
Saturated shale	51.8	10	10
Argillaceous marl	14.5	40	8
Calcareous marl	5.8	100	8
Saturated sand	3	100	30
Limestone	2	400	4
Fresh water	1.8	100	81
Dry sand	0.82	1000	4
Pure water	0.2	1000	81
Ice	0.082	10000	4
Sound concrete or sound granite	0.06	10000	6.5

Frequency domain electromagnetic method (FDEM)

FDEM method utilises two probe types:

- multi-coil probes.
- multi-frequency probes.

Depending on the chosen frequency and the coil distance in the instrument, different depths can be investigated.

As lower frequencies have higher wavelengths, they can cover a greater depth but with a lower resolution and vice-versa. The greater the separation between the coils, the deeper the penetration.

1. The multi-coil frequency domain electromagnetic probes are equipped with multiple transmitter-receiver pairs positioned at a fixed distance, each with varying separations (as depicted in Fig. 28 on the left side of the image). This design allows for simultaneous exploration of different depths at the same measurement point. Such investigations are referred to as geometrical sounding.

2. The multi-frequency electromagnetic method involves using a single transmitting-receiving pair arranged in a Slingram configuration but with the utilization of several frequencies to cover different depths (as shown in Fig. 28 on the left side of the image). This approach is known as frequency sounding.

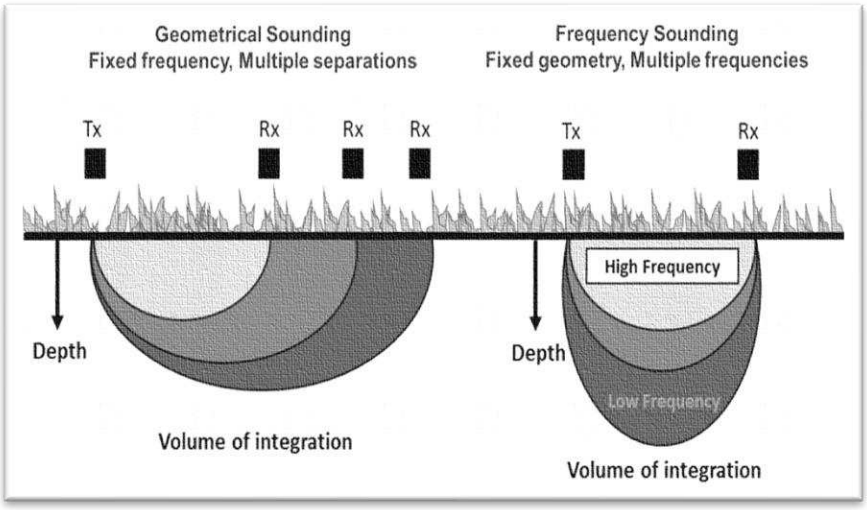

Figure 28. In the left image, multiple transmitters (Tx) and receivers (Rx) are arranged at different spacings with a fixed frequency. The right image illustrates the fixed coil distance multi-frequency electromagnetic method [34].

FDEM "Slingram" methods

Among various source-receiver combinations for FDEM methods, coplanar configuration is called "SLINGRAM". The electromagnetic Slingram method estimates the apparent resistivity of the ground simultaneously with its apparent susceptibility.

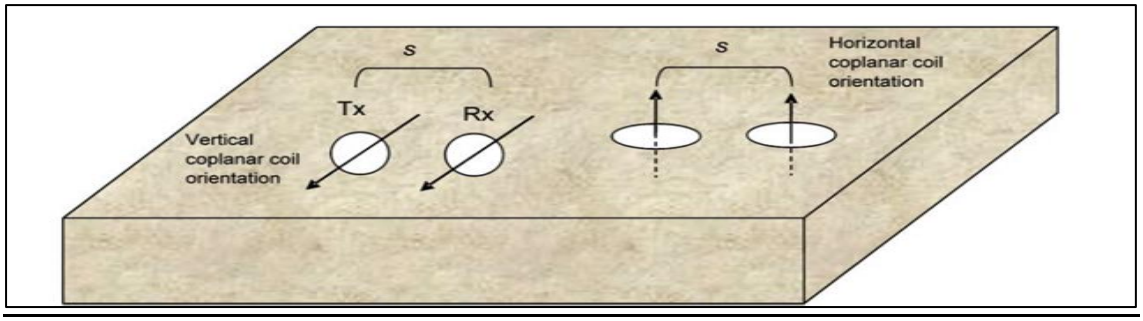

***Figure 29**: Transmitter coil (Tx), receiving coil (Rx)* [35].

Coil systems can be categorized based on the direction of their magnetic dipoles or their orientation, as described below:

1) Vertical (co-planar) coils with horizontal magnetic field (HDM OR VCP): In this configuration, the coils' axis is parallel to the ground, resulting in a horizontal magnetic dipole equivalent for the transmitting coil.

2) Horizontal coils with a vertical magnetic field (VDM OR HCP): Here, the coils' axis is perpendicular to the ground, leading to a vertical magnetic dipole equivalent for the transmitting coil. This setup provides an increased depth of investigation, approximately double that of the HDM configuration.

3) Another orientation, not utilized in our investigation, involves one horizontal and one vertical coil arranged in a perpendicular arrangement (PRP) [29].

FDEM basic principles

Based on our discussion so far, the fundamental principle of the Frequency Domain Electromagnetic (FDEM) method is based on the generation and measurement of electro-magnetic fields. It involves measuring the amplitude and phase of the secondary field with respect to the primary field.

The FDEM equipment records both components of the field signal: one is in phase with the transmitter, known as the 'in-phase' component, and the other one is orthogonal to it (90° out of phase), referred to as the 'quadrature' component. The in-phase ratio, expressed in parts per thousand (ppt), relates to the magnetic susceptibility of the ground. On the other hand, the quadrature component is linked to the ground's apparent conductivity and is typically expressed in milli Siemens per meter (mS/m). This value is an integrated measurement that depends on various soil properties such as bulk density, salinity, soil structure, moisture content, ionic composition, and more.[36]

According to our previous explanation, the frequency-domain instrument uses a continuously varying primary magnetic field Hp, produced by the electric current in the transmission coil generating an alternate current in the subsoil which in turn produces a secondary magnetic field Hs, which the receiving coil will measure.

The secondary magnetic field (Hs) is a function of source-receiver distance (s), angular frequency of our instrument ω, apparent conductivity of the subsoil (σ_a) and magnetic permeability of the medium μ ($\mu \approx \mu_0$) [36].

The conductive response from a layered homogenous subsoil structure is largely dependent on the quadrature component, and the in-phase component can be ignored [37]. Hence, apparent conductivity of the subsoil (σ_a) is defined as:

$$\sigma_a = \frac{4}{s^2 \omega \ \mu_0} \left(\frac{(\mathrm{Hs})\mathrm{Quadrature\ Component}}{\mathrm{Hp}}\right)$$

The induction number (B) is defined as the ratio of the source-receiver separation (s) divided by the plane-wave EM skin depth δ; (Thus B=s/δ) [29].

Generally speaking, skin depth (δ) is a term used in classical electromagnetics to estimate the depth of investigation for EM systems. It represents the depth at which the amplitude of a plane wave in a homogeneous half-space decreases to 1/e (approximately 37%) of its surface value. The skin depth primarily depends on the frequency of the source. If we are not in an overly conductive soil, under the low induction condition:

$$2\pi f \ll 2\sigma\mu_0 s^2$$

the skin depth can be determined as follows:

$$\delta = (\frac{2}{\omega\mu_0\sigma})^{1/2}$$

Therefore, the induction number (B) is dimensionless and can be formulated as shown:
(Low Induction Number (LIN) conditions defined as when the induction number β is <<1)

$$B = \frac{s}{(\frac{2}{\omega\mu_0\sigma})^{1/2}}$$

The vertical spatial sensitivity and effective exploration depth (*de*) of low-induction-number (LIN) instruments in layered soils were analysed using a comprehensive numerical solution based on Maxwell's equations. Previous studies, employing approximate mathematical solutions, suggested that the vertical spatial sensitivity of instruments operating under LIN conditions depends solely on the depth below the land surface, considering factors like transmitter-receiver coil separation (s), coil orientation, and transmitter frequency. However, when not under LIN conditions, the vertical spatial sensitivity and *de* are influenced by the apparent soil electrical conductivity (σ_a) and, consequently, the induction number (B). It is commonly assumed that, in most scenarios, LIN FEM instruments remain independent of the subsurface electrical conductivity.

McNeill (1980) introduced the concept of "effective depths of exploration" (*de*) based on the vertical spatial sensitivity of LIN FEM instruments in both homogeneous and horizontally layered soils. These depths were calculated using an asymptotic approximation of Maxwell's equations, with the assumption that the induction number (B) is very small. This approximation, also known as the "LIN approximation", served as the foundation for the development of numerous LIN FEM instruments [35].

Under conditions where the LIN assumptions are valid, the spatial sensitivity of LIN FEM instruments can be characterized using McNeill's cumulative sensitivity (LIN CS), which is determined as the sum of local sensitivities from infinite depth to the surface. Further details regarding LIN CS will be discussed in the following section.

The cumulative response functions.

Let us consider an EMI (Electromagnetic Induction) equipment located on the surface of a homogeneous half-space. We can visualize this half-space as being composed of an infinite number of thin layers with depth denoted by z (normalized by the inter-coil distance, s). The secondary magnetic field in the receiver coil generated by the current flowing within any of these thin layers can be calculated. McNeill (1980) formulated two functions, ΦV(z) and ΦH(z), for the vertical dipoles coil configuration and horizontal dipoles (VCP) configuration, respectively.

For the vertical dipoles configuration, ΦV(z) is represented as:

$$\Phi V(z) = \frac{4Z}{\sqrt[3]{(4z^2+1)}}$$

The function Φ describes the relative sensitivity of the two coil configurations to the material at various depths. In other words, this function describes the relative contribution of the secondary magnetic field from a thin layer at any depth, z, to the total secondary magnetic field in the receiver coil. By differentiating ΦV(z) with respect to z and setting it equal to zero, it is observed that materials at a depth of z = √1/8 provide the maximum contribution to the secondary magnetic field. Notably, near-surface materials (z close to zero) contribute minimally to the secondary magnetic field, making this coil configuration relatively insensitive to changes in near-surface conductivity.

For the horizontal dipoles (VCP) configuration, ΦH(z) is given as:

$$\Phi H(z) = \frac{2 - 4z}{\sqrt{(4z^2 + 1)}}$$

In this case, the relative contribution from near-surface material (z = 0) is maximum, and the response declines monotonically with depth.

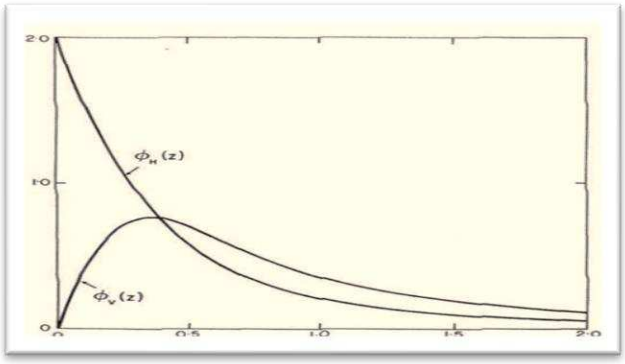

***Figure 30**: Comparison of relative responses for HCP and VCP.*

The construction of these response functions is possible due to the Low Induction Number (LIN) approximation. Under this assumption, all current flow is considered horizontal, and all current loops are independent of one another. The LIN approximation enables the definition of apparent conductivity, which is related to the secondary magnetic field measured by the receiver. The functions ΦV(z) and ΦH(z) describe the relative contributions from material at different depths to the apparent conductivity measured by the EMI instrument. Integrating the two functions from zero to infinity gives us the total secondary magnetic field at the receiver coil from the entire half-space, directly related to the electrical conductivity of the half-space. This enables precise determination of the relative influence of materials at various depths on the measured apparent conductivity when operating at low induction numbers.

To perform calculations more conveniently, McNeill (1980) introduced a function called the cumulative response function (RV|H(z)), which represents the relative contribution to the secondary magnetic field or apparent conductivity from all materials below a specified depth z. For the vertical and horizontal dipoles (VCP) configurations, the cumulative response functions can be expressed as follows:

$$R_{H}^{v}(z) = \int_{z}^{\infty} \phi_{H}^{v}(z)\,\mathrm{d}z$$

For the vertical dipoles configuration:

$$\mathrm{CS}_V = \mathrm{R}_V(\mathrm{z}) = \frac{1}{\sqrt{(4\mathrm{z}^2 + 1)}} \qquad (4)$$

For the horizontal dipoles (VCP) configuration:

$$\mathrm{CS}_H = \mathrm{R}_H(\mathrm{z}) = \sqrt{(4\mathrm{z}^2 + 1)} - 2\mathrm{z} \quad (5)$$

These equations were derived and are valid for instruments placed on the surface of the ground.

Layered Earth Model

It is a numerical model of layered soils which represents a simplified representation of the Earth's subsurface, assuming it consists of distinct horizontal layers, each characterized by constant electrical conductivity and magnetic permeability. This model is used to simulate and understand subsurface materials' behavior and their responses to electromagnetic fields.

In this model, $\sigma_k$and $\mu_k$represent the electrical conductivity and magnetic permeability of the k-th layer, respectively. The electrical conductivity describes how well a material can conduct electricity, while the magnetic permeability characterizes how a material responds to a magnetic field. Usually, $\mu_k$is considered constant if the subsoil does not contain ferromagnetic materials, which are known for their strong magnetic responses.

The goal of data inversion in this context is to determine the conductivity of each layer (k = 1, ..., n) based on the observed electromagnetic response data. This process involves solving a non-linear or linear problem using an appropriate technique, such as a least squares approach or global/local search methods.

- Thus, we define the layer thickness as dk (k = 1, ..., n),
- The dn is infinite for the nth layer, for which we have RV |H(zn) = 0
- σ_k for air is zero.
- Note that z_0 = 0, which leads to RV |H(z0) = 1,

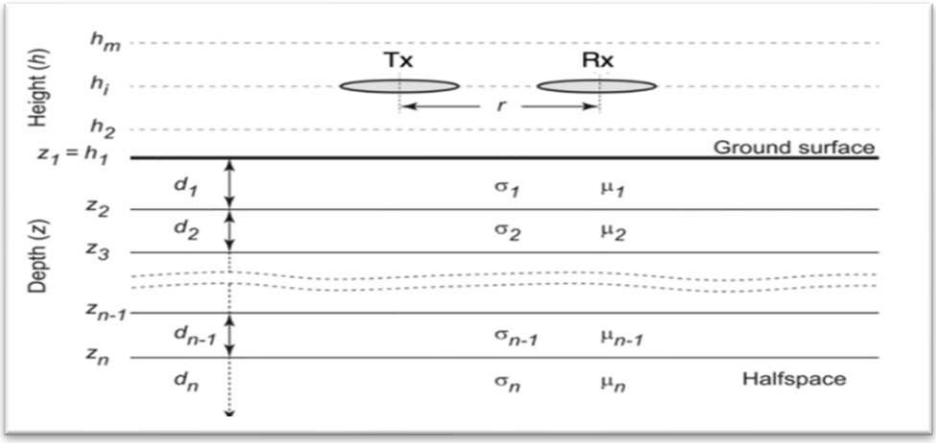

***Figure 31**: Schematic representation of the subsoil discretization commonly used in 1D* [38].

Considering the height of the coil from the ground as a variable, along with the distance between the sensors (s), these updated functions are computed as follows [39]:

$$\phi_V(z,h,s) = \frac{1}{N}\sum_{i=1}^{N} |\, d_i - f_i(m)|,$$

$$\Phi_V(z,h,s) = \sqrt{4(h/s)^2+1}\,\frac{4(z+h/s)}{(4(z+h/s)^2+1)^{3/2}}$$

$$\Phi_H(z,h,s) = \left(2 - \frac{4(z+h/s)}{(4(z+h/s)^2+1)^{1/2}}\right)\frac{1}{\sqrt{4(h/s)^2+1}-2(h\,/\,s)}$$

Accordingly, the generalized cumulative response functions are as follows:

$$R_V(z,h,s) = \frac{\sqrt{4(h/s)^2+1}}{\sqrt{4(z+h/s)^2+1}}$$

$$R_H(z,h,s) = \frac{\sqrt{4\left(z+\frac{h}{s}\right)^2+1}-2\left(z+\frac{h}{s}\right)}{\sqrt{4\left(\frac{h}{s}\right)^2+1}-\frac{2h}{s}}$$

Wait (1982) derived the Maxwell-based FS responses of an EMI instrument over a 1D-layered earth containing N layers. The mutual coupling ratio (Q), which is the ratio between the secondary and the primary magnetic field at the receiver coil as follows:

$$Q_{VCP} = Im\left(\frac{H_s}{H_p}\right)_{VCP} = Im\,(-s^2 \int_0^\infty R_0 J_1(s\lambda)\lambda\, d\lambda)$$

$$Q_{HCP} = Im\left(\frac{H_s}{H_p}\right)_{HCP} = Im\,(-s^3 \int_0^\infty R_0 J_0(s\lambda)\lambda^2\, d\lambda)$$

$$Q_{PRP} = Im\left(\frac{H_s}{H_p}\right)_{PRP} = Im\,(-s^3 \int_0^\infty R_0 J_1(s\lambda)\lambda^2\, d\lambda)$$

Im: imaginary part

J_0: Bessel functions of zeroth order, respectively

R_0: is the reflection factor, which depends on the thickness and conductivity of each layer interface between the air and the first layer and so RN+1 = 0

J_1: Bessel functions of first orders

$$R_n(\lambda) = \frac{(\Gamma_n - \Gamma_{n+1}) \,/\, (\Gamma_n + \Gamma_{n+1}) + R_{n+1} e^{-2\Gamma_{n+1} d_{n+1}}}{1 + (\Gamma_n - \Gamma_{n+1}) \,/\, (\Gamma_n + \Gamma_{n+1}) R_{n+1} e^{-2\Gamma_{n+1} d_{n+1}}}$$

$$\Gamma_n = \sqrt{\lambda^2 + i\omega\mu_0\sigma_n}$$

The above equations are, again, valid only for constant values of ϵ and μ and for the quasi-static approximation. Most electromagnetic induction equipment displays the results of measurements in terms of apparent conductivity using the LIN approximation from the imaginary part (off-phase component) of Q given by the apparent conductivity of the subsoil (σ_a) equation seen earlier.

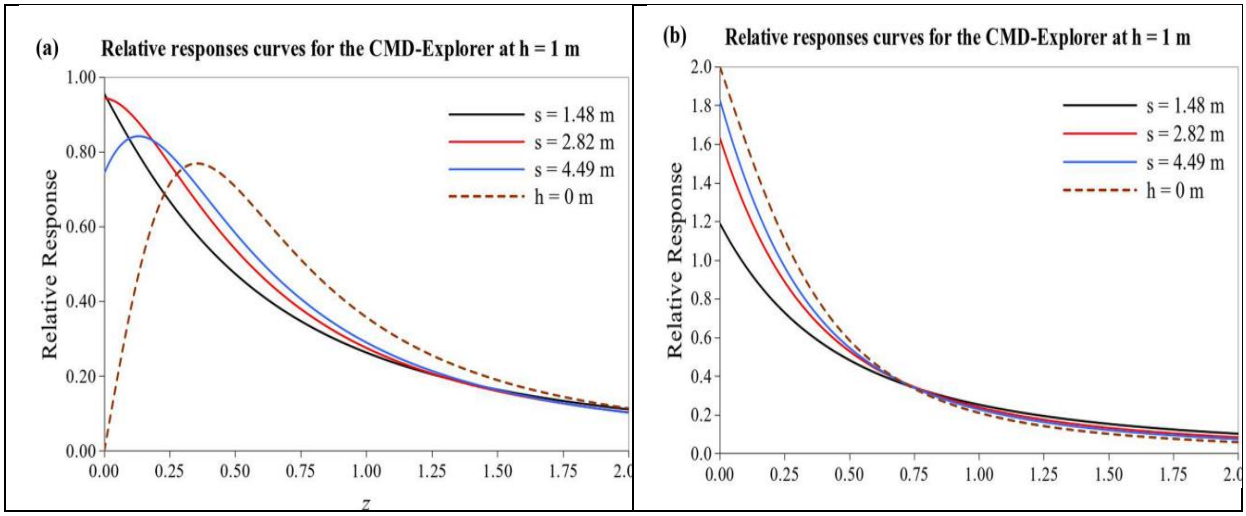

Figure 32: *Relative response curves for all possible CMD Explorer configurations at h = 1 m from the ground* [39].

Data acquisition methodology

During the data acquisition process in the field, two types of electromagnetic probe were adopted: the separated-coil FDEM electromagnetic sensor or CMD-DUO from GF-Instruments and the Multi-depth Electromagnetic Conductivity Meters or CMD-Explorer, also from GF-Instruments. The following is an explanation of their basic principles.

The CMD-DUO ELECTROMAGNETIC INDUCTION probe

The CMD-DUO electromagnetic sensor employs a transmitter (Tx) and a receiver coil (Rx) to measure subsurface apparent electrical conductivity. Adjusting the distance between the coils and using a fixed frequency can reach a specific depth. As stated in FDEM principles, by increasing the distance between the transmitter and the receiver coil, deeper depths can be reached.

Table 4*: Exploration depth for CMD-DUO Electromagnetic Conductivity Meter*

coils spacing (m)	EXPLORATION DEPTH (m)	
	Horizontal dipoles (VCP)	Vertical dipoles (HCP)
10	7.5	15
20	15	30
40	30	60

Another important factor is the orientation of the coils. In the VCP configuration, both the transmitting and receiving coils are oriented vertically, and in the HCP configuration, the transmitting and receiving coils are oriented horizontally. Changing the orientation of the magnetic dipole from VCP to HCP can increase the depth of exploration. This is because the HCP sensitivity distribution reaches its peak at greater depths than the VCP distribution.

A sensitivity function describes how changes in subsurface properties (electrical conductivity) affect the measured EM response for different coil configurations. As shown in the next figure, measurements acquired with coils in the VCP mode are more sensitive to the shallow subsurface. By contrast, measurements acquired in the HCP mode are more sensitive to deeper depths.

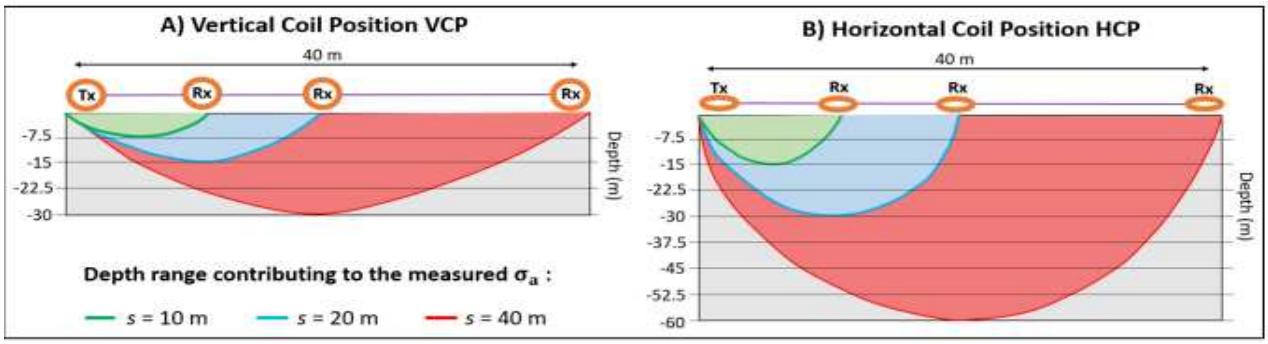

***Figure 33**: A) CMD-DUO Nominal depth range for s= 10, 20, 40, using the vertical coil orientation (VCP). B) with the horizontal coil orientation (HCP).*

Again, here we can see the depth as a function of normalized sensitivity for vertical and horizontal configurations:

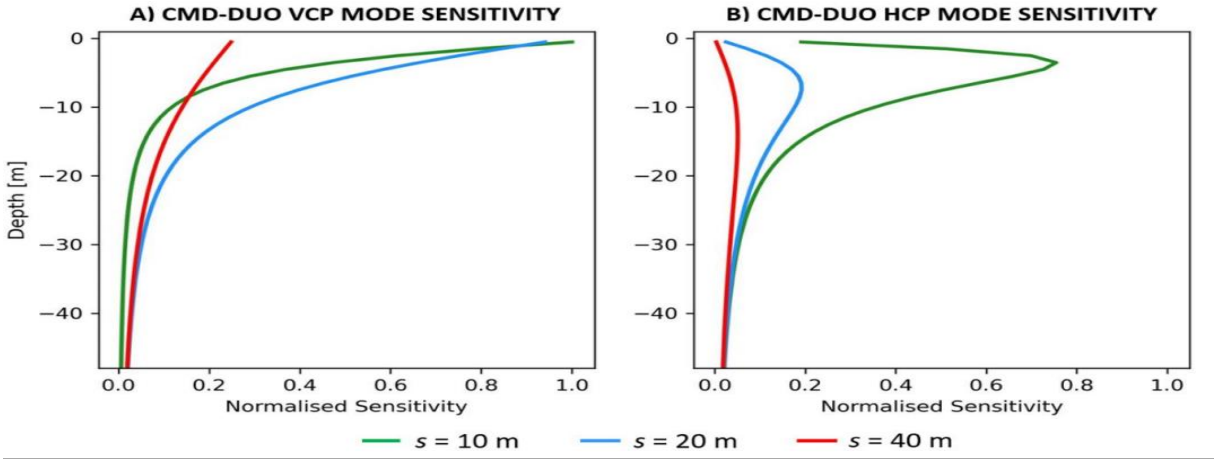

***Figure 34**: A) CMD-DUO normal sensitivity to depth for s= 10, 20, 40, using the vertical coil orientation (VCP). B) with the horizontal coil orientation (HCP).*

***Figure 35**: The main components of the CMD-DUO.*

CMD EXPLORER – Multi-depth Electromagnetic Conductivity Meters

The CMD Explorer is a multi-receiver coil sensor designed for near-surface conductivity studies. It can operate at a specific frequency and employ different coil spacing to investigate various depths. Accordingly, this instrument can collect several apparent conductivity ($\boldsymbol{\sigma a}$) values by employing both Horizontal Dipole Mode (HDM OR VCP) and Vertical Dipole Mode (VDM OR HCP) configurations for each depth. The HDM and VDM configurations involved transmitting and receiving electromagnetic signals in different directions, providing complementary data of the subsurface. The coil orientation can be changed from vertical dipoles (Horizontal Co-laner) to Horizontal dipoles (Vertical Co-planner) by rotating the probe tube through 90º.

***Figure 36**: The main components of the CMD-EXPLORER.*

The instrument is designed with low coil separation distances ideal for shallow investigations. The high sensitivity of the instrument at low depths makes it ideal for near-surface studies.

The technical specifications of the multi-coil CMD Explorer are:

***Table 4**: Technical specifications of the multi-coil CMD Explorer*

Probe **CMD-Explorer**	Effective High/Low Depth Range.	Dipole Centre Distance	<u>Weight</u> **8.0 kg**	<u>Frequency</u> **10 kHz**
	2.2 / 1.1 m	1.48 m		
	4.2 / 2.1 m	2.82 m		
	6.7 / 3.3 m	4.49 m		

During the investigation of the Sella Group Mountain, the CMD Explorer was utilized to explore the subsurface conductivity properties, employing both Horizontal Dipole Mode (HDM) and Vertical Dipole Mode (VDM) configurations.

Data Acquisition

The First Case study (Sella group mountain glaciers)

ERT method

Table 5. provides all the necessary information regarding the Sella group rock glacier acquisition procedure. Both case studies in Alpine Mountain were conducted using the same survey setup.

In Murfreit, the investigation line was oriented longitudinally along the development of the rock glacier, covering a total length of 70.5 m. Murfreit's data acquisition was conducted in July 2020.

On the contrary, the investigation line performed on the rock glacier of Piz Boé was defined orthogonally to the rock glacier development. Data acquisition for Piz Boé Glacier was performed in September 2020.

***Table 5**: ERT survey acquisition parameters*

Instrument	MAE Digital Geo-resistivimeter
Power Supply	60 A-12 V External battery
Configuration	Dipole-Dipole skip 0
Current Injection Time	250 ms
Stack Max	6
V Min	0.001 V
V Max	800 V
Electrodes Number	48
Spacing	1.5 m
Array Length	70.5 m

FDEM METHOD

In the case study of the Sella Group mountains rock glacier, the FDEM measurements were performed on the same investigated lines of the ERT surveys.

The investigation was carried out using a CMD-Explorer probe by Gf-instruments employed with the instrument limit (accuracy) of 0.1 mS/m and it was maintained relatively fixed at the 1m height from the surface (this device's characteristics are described in the following Table 4).

Both horizontal and vertical orientations were employed. The survey was repeated multiple times in order to reduce possible air temperature drift.

The shortest separation distance (1.48 m) was affected by a minimal amount of scattering which did not affect probe separations with longer inter-coil distances primarily due to their depth of investigation.

As stated before, in FDEM the depth of penetration is related to the separation between the coils. Longer probes have a larger coil separation, which allows them to probe deeper into the subsurface. Thus, the shortest probe with the smallest coil separation is more sensitive to near-surface effects. Any scattering or instrumental drift occurring in the uppermost part of the ground has a more noticeable influence on the measurements collected by the shortest probe.

CMD-Explorer probe has three different inter-coil distances and two possible coil configurations of Horizontal and Vertical mode. As a result, six apparent conductivity values can be obtained.

As we discussed before, we defined two different sensitivity functions for HCP and VCP.

The vertical coil orientation was more sensitive to shallower depths, while the HCP orientation was more sensitive to deeper depths.

The instrument was set at a fixed frequency of 10 kHz. It consists of three pairs of coils separated by 1.48 m, 2.82 m, and 4.49 m.

It is important to take into account the sensitivity pattern shift caused by the probe's height above the surface. To achieve the best possible results, the instrumentation should be kept at a constant height relative to ground level, in order to avoid significant variations in the measured data. The probe was kept at a distance of one meter during the acquisition phase in order to satisfy this requirement.

***Figure 37**: Electromagnetic Measurements Using the CMD-Explorer at the Piz Boé Rock Glacier Site. Photo by Boaga, 2020*

The Second Case study (Calderone Glaciers)

The Calderone Glacier study involved the application of the FDEM method in combination with GPR due to the presence of several meters of snow cover. This limited the use of Electric Resistivity Tomography (ERT) and active seismic methods.

The GPR method

The Calderone Glacier data collection was conducted on snow cover using a GSSI Sir4000 instrument with a 200 MHz digital antenna.

The table below summarises all the necessary information regarding the GPR survey acquisition procedure and parameters.

***Table 7**: GPR survey acquisition procedures and parameters*

Survey Type	GPR (March 2022)			
Glacier	Calderone Glacier			
GPR instrument	GSSI Sir4000, 200MHz digital antenna			
Acquisition Parameters	Range:400	Samples:1024	sample/sec:40	Dynamics:32(bit)
Georeferencing	Trimble R9s GPS receiver in RTK configuration			
Depth conversion (avg. EM speed)	Snow cover: 0.201 m/ns - Ice layer: 0.1682 m/ns			

The FDEM method

The FDEM measurements on the Calderone glaciers were performed using a CMD-DUO probe by Gf-Instruments because of its high-depth penetration capabilities. That operated at a low transmitted frequency of 925 Hz with three relatively large coil separations of 10, 20, and 40 meters. Both vertical coil orientation (VCP) and horizontal coil orientation (HCP) modes were employed to obtain multiple conductivity values at each measurement point. For every measured point, which is considered to be halfway between the two coils, six apparent conductivity values can be obtained.

With regard to the acquisition line (Figure 38), both GPR and FDEM data were acquired along two investigation lines, one longitudinal (line 1) and one orthogonal to the development of the glacier (line 2).

Table 8: FDEM acquisition information.

Measurement Type	FDEM
Glacier	The Calderon Glacier
FDEM Instrument	CMD-DUO probe by Gf-Instruments
Transmitted Frequency	925 Hz
Coil Separations	10, 20,40 m
Coil Orientations	Both VCP and HCP
Measurement Points	Conductivity (σa) values (halfway between the coils)
Acquisition Lines	Longitudinal (Line 1), Orthogonal Line to the glacier's development (Line 2)

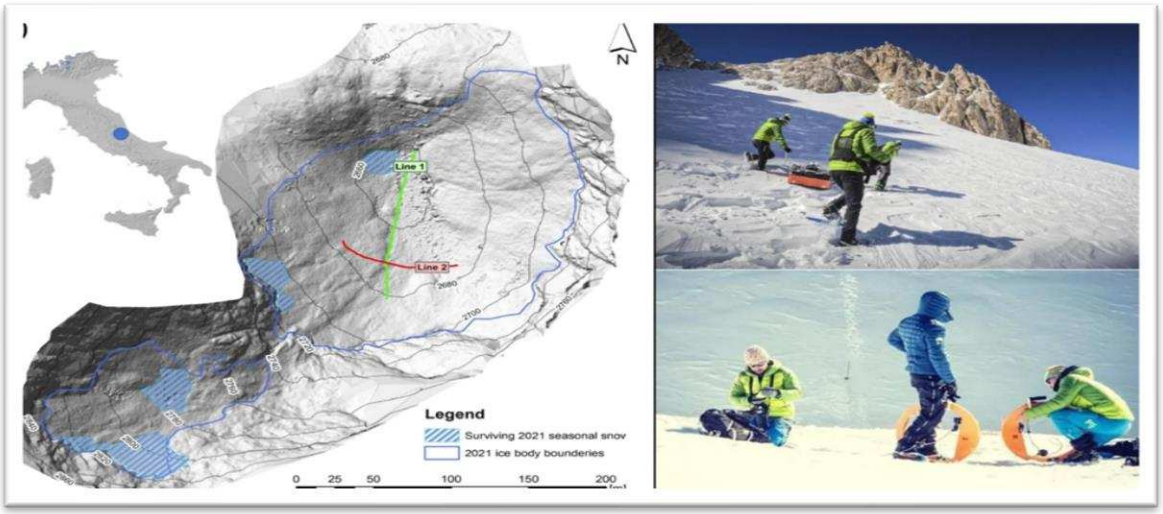

Figure 38: Calderone acquisition lines and instruments.

Data inversion and processing

The electromagnetic collected data was processed using open-source Python-based software called "EMagPy". In this chapter, data inversion procedures are discussed in detail.

Forward modeling

To create an inverse model, it is essential to have the capability to produce a forward model as a starting point. In other words, before attempting to invert or estimate the parameters of the subsurface, you need to be able to calculate the predicted response of the forward model given a set of input parameters.

Once you have a reliable forward model, you can use it to generate synthetic data by simulating the response for different sets of input parameters representing the subsurface properties. These synthetic data can then be compared with the actual observed data acquired in the field during geophysical surveys.

The goal of inverse modeling is to adjust the model parameters iteratively until the forward-modeled response matches the observed data as closely as possible. This process involves optimization algorithms such as CS and LBFGS, which update the model parameters based on the comparison between the predicted and observed data.

As explained in the last chapter, Linear Cumulative Sensitivity (CS) Functions were proposed by McNeill in 1980 as a method to analyze the sensitivity of electromagnetic data to changes in subsurface conductivity in a linearized manner.

The linear CS functions provide valuable insights into how specific frequencies contribute to resolving subsurface conductivity variations. They allow for an approximate but computationally efficient assessment of sensitivity.

This algorithm is still common, especially when dealing with relatively simple subsurface structures or when computational efficiency is a primary concern. As explained, these CS functions assume that the sensitivity of the instrument is only a function of depth and coil separation, and the instrument is working under LIN conditions.

On the other hand, non-linear full solution (FS) forward models are based on solving Maxwell's equations. Unlike the linear CS functions, these models provide a more accurate representation of the subsurface response to the electromagnetic field and are not limited to linear approximations.

The complexity of Maxwell's equations makes it more computationally demanding, especially when considering 2D or 3D models. However, they offer higher accuracy and are essential for accurately modeling complex geological scenarios, especially when the subsurface contains highly conductive or resistive bodies.

Therefore, FS forward models must be used to calculate a non-simplified ground response, in terms of HS/ HP. As stated before, we can use Wait's (1982) equations for the Maxwell-based FS responses of an EMI instrument over a 1D-layered earth containing N layers.

In EMagPy, FS forward models are used based on the assumption that electromagnetic fields propagate only through conduction currents.

Inversion Basic principles

This section provides an overview of the inversion procedure in general and with particular reference to EMagpy software that was used for the inversion of FDEM data.

In general, two types of inversion methods are available: deterministic and probabilistic.

- Deterministic Inversion:

Deterministic inversion methods seek a single "best" solution by minimizing an objective function. These methods are often based on gradient-based optimization techniques. The goal is to find the model that best fits the data. Parameters value iteratively adjusted till satisfactory model fit.

In linear forward models, the Jacobian matrix (sensitivity matrix) can be computed directly, simplifying the inversion process. However, when using more complex forward models (FS forward models) the problem needs to be linearized to calculate the Jacobian matrix efficiently.

Deterministic inversion is relatively fast and computationally efficient. But if we are looking for a more precise method the probabilistic inversion is a better option.

- Probabilistic Inversion:

Probabilistic inversion methods focus on characterizing the uncertainty associated with the inferred subsurface parameters. Instead of providing a single solution, they produce posterior probability distributions for the model parameters. This method provides a range of possible solutions, despite being more computationally demanding, thus allowing for better uncertainty quantification [40].

Inverse Problems and Regularization:

Inverse problems involve estimating unknown subsurface properties or parameters from observed geophysical data. Due to the inherent noise in real-world data and the ill-posed nature of many inverse problems, the solutions can be unstable and sensitive to noise. Regularization techniques are employed to stabilize the inverse solutions by introducing a penalty term that discourages excessive parameter variations. This helps control the trade-off between fitting the data and preventing overfitting.

The L-Curve: The L-curve is a plot where the norm of the model solution (often the vertical axis) is plotted against the norm of the data misfit (often the horizontal axis) for a range of regularization parameters. The L-curve helps practitioners find the regularization parameter that corresponds to

the corner of the curve, which strikes the right balance between fitting the data and maintaining a stable solution. This parameter choice results in a solution that captures the essential features of the subsurface without being overly influenced by noise.

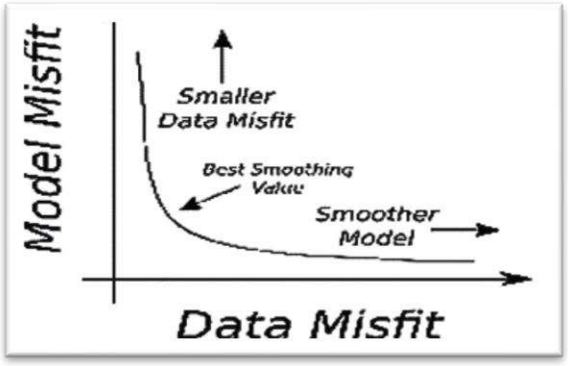

Figure 39. *L-curve which will plot a graph of model and data misfit for a number of vertical smoothing values.*

Model misfit

Data misfit refers to the difference between observed values and predicted values determined by the forward model. The total misfit is given by:

$$\Phi = \Phi d + \alpha \Phi m$$

α: Regularisation or smoothing parameter.

αΦm: smoothing term.

Φm: the model misfit term, quantifying the smoothness or simplicity of the model.

Φd: the data misfit, measuring the difference between observed and predicted data.

In EMagPy the inverse problem can be solved by sharp or smooth variations on the model.

Regularization in inversion is used to control the complexity or smoothness of the resulting model. regularization parameter plays a crucial role in finding an optimal balance between data misfit and model complexity [40].

Regularization Parameter in Smooth Inversion:

Smooth inversion typically produces a model with more EC values than measurements. This model must be regularized with a model misfit term to determine the smoothness of neighboring layers. By adjusting the regularization parameter α, the inversion algorithm can control the trade-off between fitting the observed data and producing a smooth model.

Larger α values will emphasize the smoothness of the model, whereas smaller α values will prioritize fitting the data more precisely.

Regularization Parameter in Sharp Inversion:

In the sharp inversion, both conductivities and depths are parameters of interest. The problem is typically over-determined, meaning there are more measurements than parameters to be estimated. In this case, the model is under-constrained, and various solutions can fit the data equally well. In this case, Φm will be set to zero and the total misfit (Φ) is solely governed by the data misfit term (Φd), which measures the difference between observed and predicted data.

As stated before, Φd is the data misfit which measures the difference between observed and predicted data. It can be obtained using L1 or L2 norm objective functions [40].

The L1 norm objective function is based on absolute differences. The data misfit for L1 norms can be written as:

$$\phi_d = \frac{1}{N}\sum_{i=1}^{N} | d_i - f_i(m)|,$$

L2 norm (least squares norm) objective function is the sum of weighted, squared differences between predicted and observed values can be written as:

$$\phi_d = \frac{1}{N}\sum_{i=1}^{N} (d_i - f_i(m))^2$$

N: number of coil configurations per profile.

D: the observed values (data).

f(m): predicted values from the forward model with parameter m.

Optimization methods in EMagPy

EMagPy provides some methods to minimize the total misfit during the inversion [40].

The Gauss-Newton involves obtaining the Jacobian (sensitivity) matrix. This method is straightforward for CS forward models due to their linear nature, as sensitivity is not dependent on electrical conductivity (EC).

For the FS forward models, the sensitivity is calculated for an assumed subsurface EC and if the initial EC model does not match the data well, the solution can perform poorly.

The Gauss-Newton requires fixed depths and a large α value to produce smooth solutions. As the Jacobian matrix for the CS forward model does not depend on the layer conductivity, the solution is reached in one iteration.

For the FS forward model, the Jacobian matrix can be updated for each iteration until the solution reaches convergence, which is a relatively quick process.

As explained before, the FS forward models can be modified to account for cases when the device is operated above the ground, and in EMagPy this is done by modeling the 'air gap' as a layer with an EC of 0 mS/m, the same approach is also used for the CS functions.

ERT inversion summary

The purpose of this thesis is not to focus on ERT processing or provide detailed ERT processing explanations. Rather, it provides a brief overview of the steps taken in ERT processing (for both case studies) within the Sella mountains. The ERT models are used as a reference point to compare them with the data from the FDEM.

***Table 9**: The study case of Sella group mountain data inversion and processing summarised information.*

Study Case	**Murfreit**	**Piz Boé**
Date of Survey	July 2020	September 2020
Data Thresholds	AV ≥ 1 mV	AV ≥ 1 mV
Quadrupoles Saved	≥ 90%	< 50% (after reciprocity check applying a threshold of 20%)
Reciprocal Check	< 10% variance	All direct and reciprocal measurements used
Inversion Code	R2 (based on Occam's inversion method)	ResIPy (Python GUI for R2)
Error Model	Not specified	Power law error model (using all direct and reciprocal measurements)
Number of Iterations	3	2
Final RMS (Root Mean Square)	RMS < 1	RMS < 1

SELLA group case study FDEM inversion and processing

We used EMagPy open-source software for the processing of both study sites.

FDEM forward and inverted modeling

As stated before, A forward model is essential to simulate the expected responses of subsurface structures based on known geologic conditions. This mathematical model takes into account the physical properties of the subsurface, the geometry of the measurement setup (transmitter-receiver configuration), and the characteristics of the geophysical instrument being used. By inputting the known conductivities of the subsurface and the geophysical survey setup, the software calculates the expected measurements that would be recorded by the instruments. By comparing the predicted responses from the forward model to the field-acquired data, we can assess the accuracy and verify the obtained results.

For the multi-coil CMD Explorer Frequency Domain Electromagnetic (FDEM) method with the fixed frequency of 10kH and inter-coil distances of 1.48m, 2.82m, and 4,49m (refer to Table 6.), using both VCP and HCP modes and considering a layered earth model comprising four distinct layers, each characterized by conductivity values from literature (similar to table 10 values). Applying the Cumulative Sensitivity (CS) function with a 2% noise level. For the inverted synthetic model, we used a 20-layer model with a thickness of 0.4m and an initial conductivity value of 1. We obtained the L-curve which helps determine the right level of regularization, then with the use of the CS forward model solution, and the L-BFGS-B (Broyden–Fletcher–Goldfarb–Shanno) an optimized model was made. FDEM synthetic forward models were calculated to be compared with the results of the inverted FDEM field dataset.

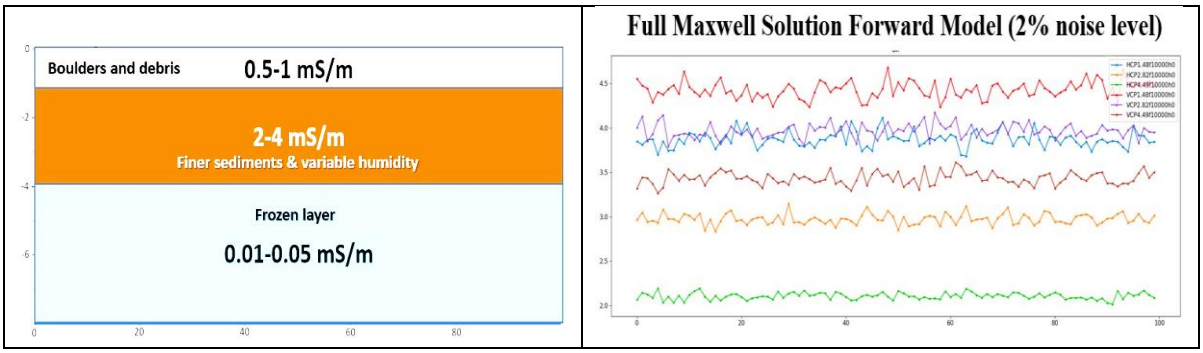

***Figure 40**. Forward modeling*

It is important to consider the instrumental resolution limit. conductivity values found with the FDEM instrument will be estimated differently from the Real values If the conductivity range goes beyond the instrument resolution. This is due to the intrinsic instrumental resolution limit of the FDEM equipment in highly resistive environments. In fact, in the rock glaciers, the values of resistivity commonly range between 10^3 and 10^6 Ωm, so the response might go further than the resolution limit of the FDEM instruments (for the CMD-Explorer ~0.1 mS/m).

Therefore, forward modeling helped us to overcome the instrumental limit. We used the forward model to define the boundary of the frozen layer, which was then used in our inverted model.

During the inversion step, the denoised field data was imported and further enhanced by applying additional smoothing on the data using the Rolling Mean method. (Which helped us to get a better image at the end). Subsequently, by utilizing the CS function and the L-BFGSB optimization method, we successfully achieved the final inverted model, resulting in a Relative Root Mean Squared Error of 1.36.

Once the inversion was completed, it was necessary to apply a correction factor of 0.01. This adjustment was essential to achieve alignment with the scale of our synthetic model. Finally, further refinements were made by zeroing out the color scale (the conductivity range).

FDEM Forward and Inverted Modeling

Once again, we used the EMagPy software to follow the same steps for making a forward and inverted model for the Calderone glacieret case. Our main goal, as always, is to make sure the forward-modeled data closely match the inverted results.

For the forward modeling of the CMD Multi-depth Electromagnetic Conductivity Meter (GF-Instrument) with a fixed frequency of 925kH and coil distances of 10m, 20m, and 40m (refer to Table 4.), using both VCP and HCP modes. again, considering a layered earth model comprising five distinct layers, each characterized by conductivity values from literature and information from the 2015 GPR survey. (Similar to Table 10 values). To simulate the non-simplified response of the CMD-DUO survey, the Full Maxwell Solution has been used with a noise level of 2%. For the inverted synthetic model and inverted model, we used a 30-layer model with a thickness of 1.3m and a starting conductivity value of 1 to obtain the L-curve which helps determine the right level of regularization, then with the use of the CS forward model solution, and the Gauss-Newton optimization FDEM synthetic forward models were calculated to be compared with the results of the inverted FDEM field dataset. In order to create an accurate subsurface representation, the actual topography of the area needed to be added to both the inverted synthetic model and the inverted model to create an accurate subsurface representation. In this regard, we used MatLab codes to align the topography with our model.

To summarize some key points:

- FDEM data must be interpreted carefully due to the limit of instrumental resolution.
- Forward modeling is recommended for reliable interpretation of inversion results, aided by filtering and smoothing of the dataset.
- Use of the CS function and Gauss-Newton optimization method helps reduce computational effort and achieve a quasi-2D conductivity model.
- Complex inversion methods based on Maxwell's laws are possible but may show minimal differences in low electrical conductivity environments.

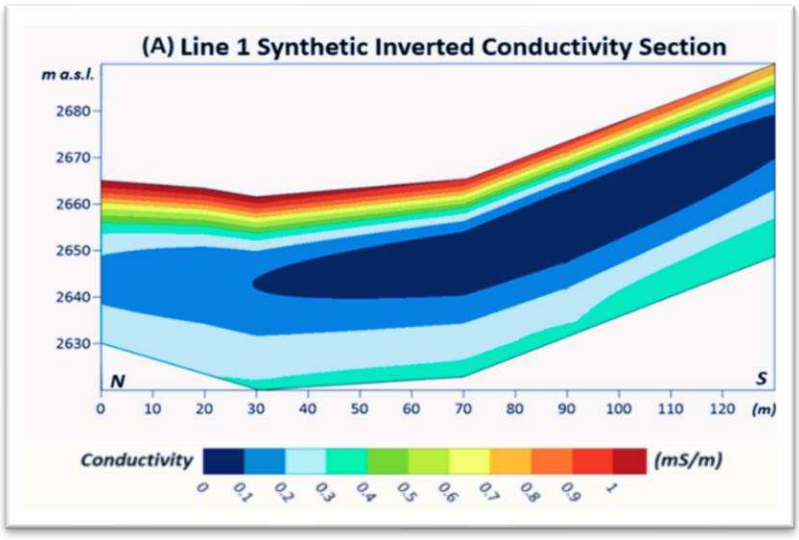

***Figure 41**.Synthetic inverted model (Including topographic information).*

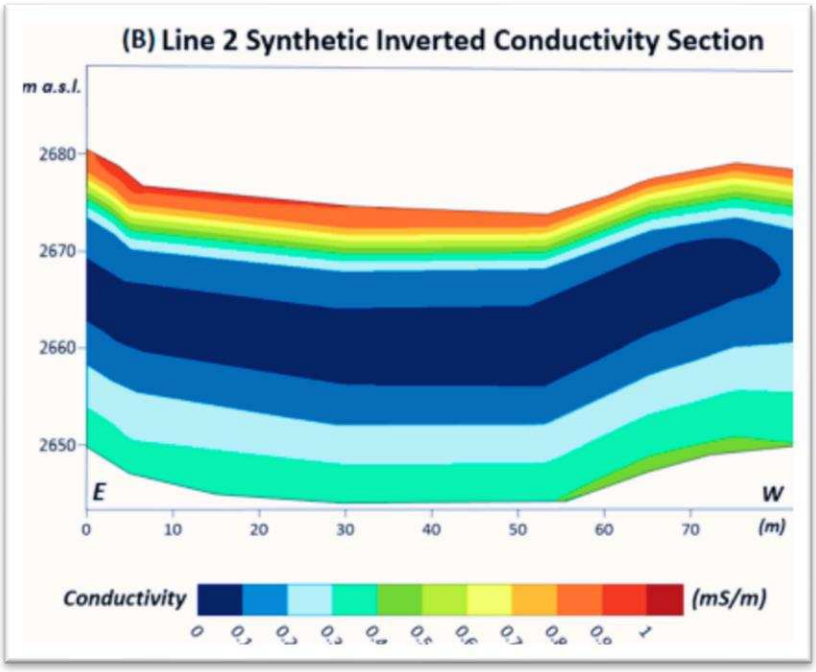

***Figure 42**. Synthetic inverted model (including topography data).*

Due to the complex geological conditions, two distinct forward models had to be made with the same parameters. Subsequently, these models were combined either using Excel or a MatLab code to generate the ultimate forward model. This final forward model served as the basis for constructing the inverted synthetic model in the subsequent stages.

The forward modeling procedure does not consider any instrumental resolution limit. Nevertheless, as mentioned before, the CMD-DUO has an instrumental limit of 0.1mS/m. Consequently, in the results of the inverted FDEM field dataset, we did not expect to find conductivity values in the same range as the synthetic models. Despite this, the sub-surface structures defined with the synthetic FDEM models are very similar to the results found with our field datasets. Yet, a shift of two orders of magnitude(10^{-2}) is required to align the conductivity values. (This adjustment is facilitated by the utilization of MatLab codes.)

Following the conductivity correction, we proceed with shifting the elevation to zero using a MatLab code. Subsequently, we employed the Surfer software to carry out interpolation and adjust conductivity color scales.

Here is a table of the electrical conductivity values (from the literature) used to perform the forward modeling process in the Calderone survey (along with the 2015 GPR survey).

***Table 10**: Conductivity References from Literature.*

Conductivity (mS/m)	Snow	Frozen calcareous Debris	Ice	Bedrock
	1	0.02	0.001	0.2

Result and discussion

We used EMagPy open-source software to make a model for two different data sets from the Sella group mountain and Calderone glaciers.

The software implements the modules required for building an inversion method: forward modeling, optimization, and regularization. We used these modules to develop an inversion model to estimate the depth of the ice core in Calderon glaciers. We also estimated the thickness of the active layer and the presence of the ice layer in the Piz Boé and Murfreit mountains. Having the FDEM inverted model, we were able to compare the model with ERT and GPR results to determine to what extent the FDEM instruments can be effective in such a frozen and highly resistive environment. Following that, we will describe the results obtained for every examined location using the respective techniques and compare them with the FDEM model.

Case study of the Sella group

The ERT results

Based on the number of publications in recent years, the ERT is considered to be one of the most widely used geophysical methods for studying mountain permafrost.

The following figure presents the inverted resistivity sections of Piz Boé rock glaciers obtained from the datasets collected with ERT. It should be noted that the ERT resistivity sections cut at a depth of eight meters to be comparable with FDEM conductivity sections that do not reach deeper than this depth. while ERT can achieve greater depth by increasing the skip of electrodes, our primary objective here was to facilitate a direct comparison with the CMD-explorer FDEM instrument, hence the utilization of the skip one configuration.

As stated, our objective was to verify the presence of the frozen soil and the active layer thickness (ALT) and find the boundary between unfrozen and frozen debris.

Resistivity values greater than 10^5 were assumed as the presence of frozen material and presumed compact ice bodies and the values less than 6×10^4 Ωm have been attributed to the presence of non-glacial and dry debris deposits and the values between these two values are considered as active layers or partially frozen layers.

The resistivity section of the Piz Boé indicated the presence of the active layer at depths varying between 2 m and 4 m followed by a continuous ice layer that extends to greater depths. As explained, having the inverted image up to the eight-meter depth we are unable to define the thickness of the ice layer as it reaches much deeper than this depth.

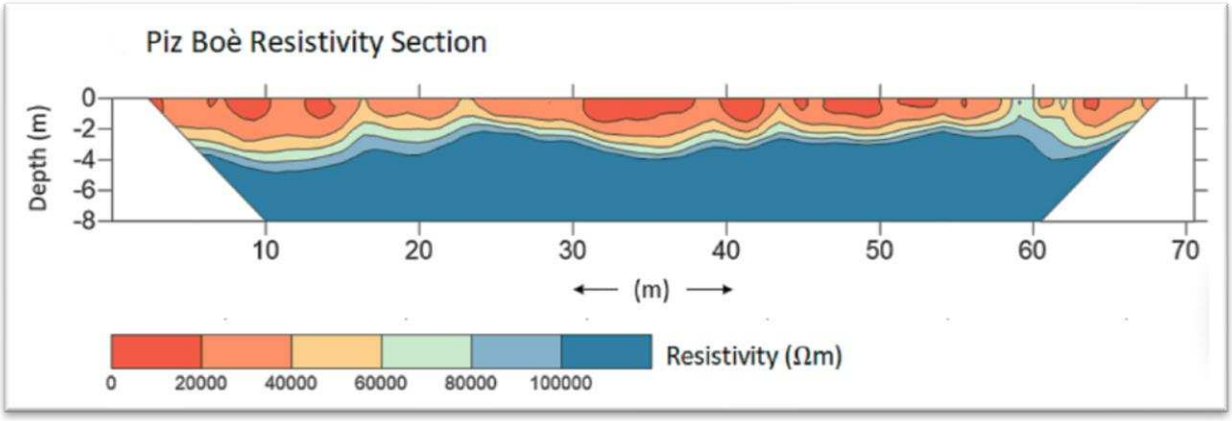

***Figure 43**.Figure 42: ERT resistivity section obtained for the Piz Boé rock glacier site.*

The figure below illustrates the inverted resistivity sections of the Murfreit rock glaciers, obtained from the datasets collected with ERT. The ALT at the Murfreit site is estimated to range from 1.5 to 3 m in the first part of the section. The central area is characterized by rocky material mixed with ice, the active layers and compacted ice layer are concentrated before the 40 m point and fade away towards the end of the investigation line. Therefore, lower resistivity values present beyond this point indicate the absence of a frozen layer extending across the initial 40 meters of the surveyed line (up to the 8-meter depth). As a result, only ice-free debris can be identified from this point afterward until the end of the investigation line.

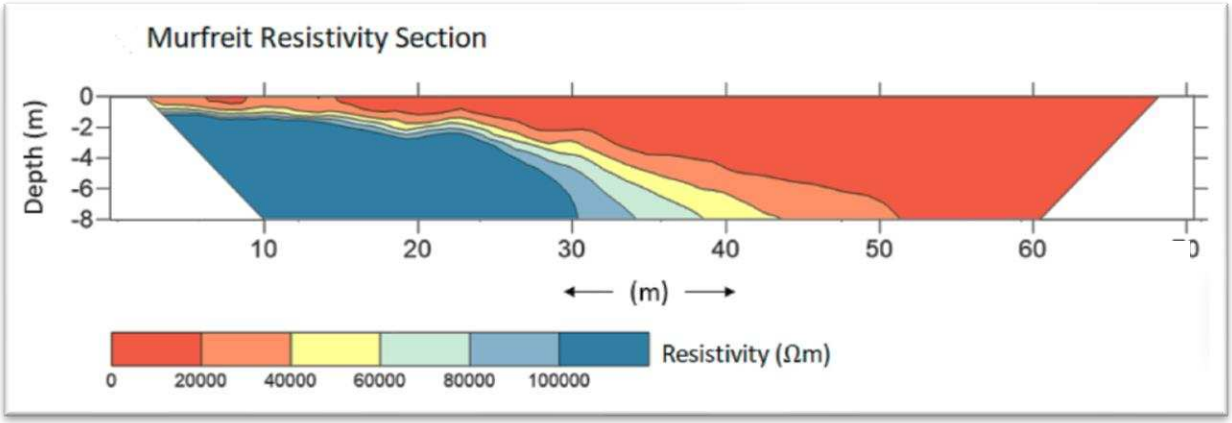

***Figure 44**.Figure 45: ERT section of resistivity obtained for the Murfreit rock glacier site.*

The FDEM results

The conductivity profiles obtained from FDEM data inversions exhibit a striking similarity to the electrical property distribution observed in the corresponding ERT sections.

As previously discussed, mountain permafrost regions exhibit a notably high resistivity range (10^3 Ωm to 10^6 Ωm). Consequently, the response exceeds the resolution capacity of FDEM instruments. To ensure an accurate assessment of the collected data, a correction factor of 0.01 was implemented in the inverted conductivity model. However, it should be noted that, due to the very low conductivity value in these settings, the LIN condition is practically always satisfied.

As stated before, the capabilities of the CDM Explorer are insufficient to reach greater depths. Thus, the bedrock-ice layer boundary cannot be determined. Nonetheless, it's important to note that our primary objective here wasn't focused on defining ice layer thickness or finding the bedrock boundary. (However, in our second case study or Calderone research, our main goal was to determine the maximum thickness of the ice layer. We successfully reached the desired depth using the CMD-DUO FDEM instrument, which offered greater depth capabilities compared to the CDM Explorer).

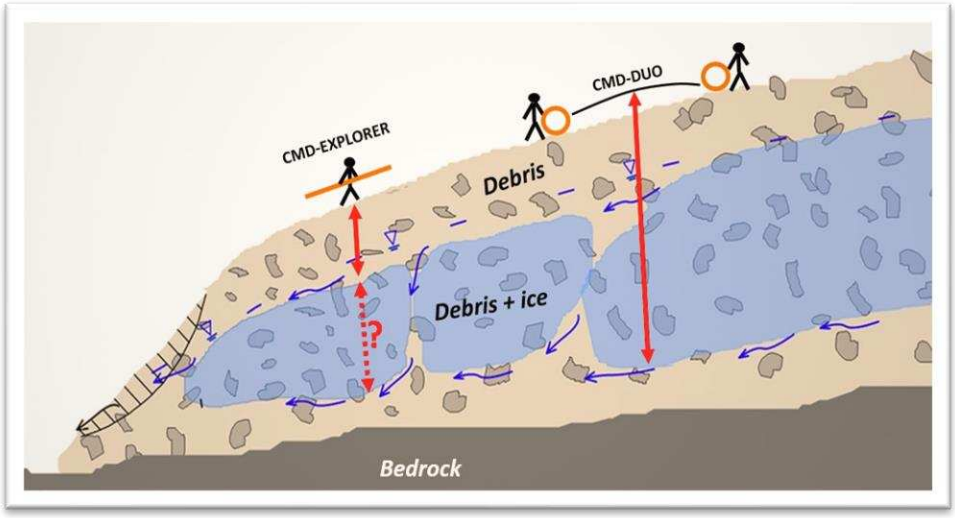

***Figure 45**. Depth of investigation for two different FDEM instruments the left one or CMD-EXPLORER employed in Sella group mountain and the right one or CMD-DUO in Calderone Glacieret.*

The Piz Boé rock glaciers conductivity map

In the conductivity section of the Piz Boé site (Figure 46), a distinct pattern is evident. Notably, lower conductivity values are consistently found at depths ranging between 3 m and 4 m. This observation aligns well with the Active Layer Thickness (ALT) estimated from the corresponding resistivity section. The conductivity profiles obtained from FDEM data inversions closely resemble the electrical method resistivity distribution in the corresponding ERT sections (See Fig 43).

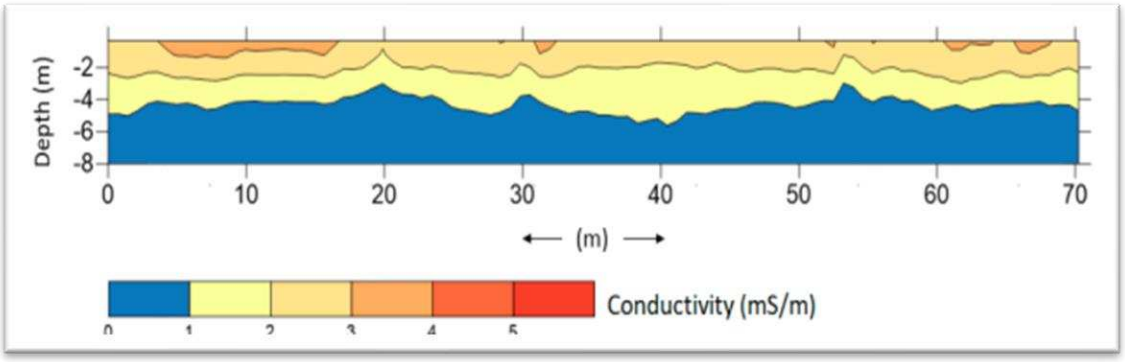

***Figure 46**.Piz Boé Inverted conductivity model.*

The Murfreit rock glaciers conductivity map

The conductivity section of the Murfreit rock glacier reveals an interesting trend. Lower conductivity values (<1 mS/m) are primarily confined to the initial 40–45 m of the investigation line. This pattern is in accordance with the subsurface structure identified through the corresponding ERT survey. The FDEM data inversions of conductivity profiles for the Murfreit site have also a similar result to the findings from the ERT sections. In the following image 47 we can see a strong correspondence between the two methods (See Fig44).

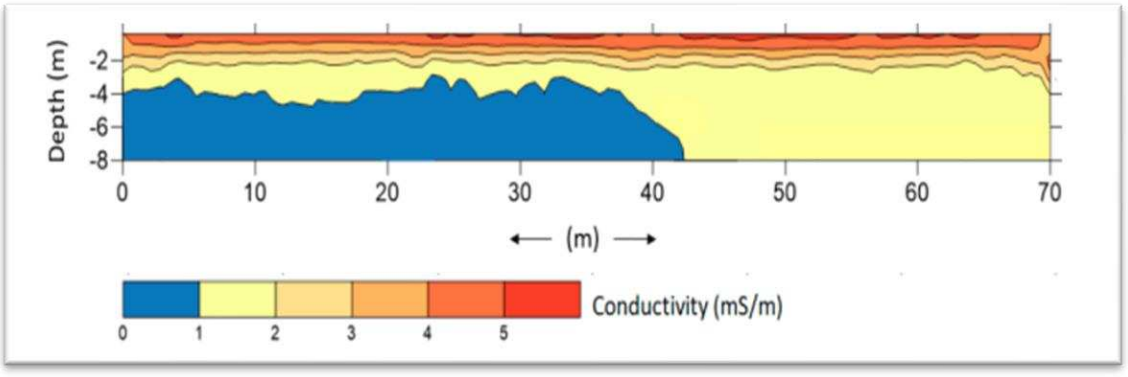

***Figure 47**.Murfreit inverted conductivity model.*

Interpretation of the results

Comparing the FDEM results with those from ERT and boreholes in the Sella Group mountains, we were able to successfully determine the Active Layer Thickness (ALT) and identify the boundaries between frozen and unfrozen regions in both studied sites. However, due to limitations in the CMD-explorer equipment, we were unable to reach the bottom of the bedrock. Despite this limitation, FDEM allowed us to distinguish the boundary between ice and debris and effectively identify the active layer which is essential to the risk management in the area.

This sudden absence of electrical values attributable to frozen soil suggests that the front part of the Murfreit rock glacier is experiencing thawing. The thawing process could have significant implications, including the potential release of dangerous debris. This finding aligns with the previous surveys which reported instances of hazardous debris releases in similar thawing conditions.

In contrast, the measurements taken at the Piz Boé site present a different scenario. The ALT at this site was found to be constant, measuring around 3–4 meters. This stable ALT is supported by the presence of a massive ice layer characterized by high-resistivity values. Furthermore, the ERT surveys conducted in 2011 in the vicinity of our research area also confirmed this constant ALT, suggesting that the rock glacier at Piz Boé is in a steady condition. Unlike the Murfreit rock glacier, there is no expected loss of ice due to temperature increase at Piz Boé.

The stable condition at Piz Boé may be attributed to the unique nature of this debris-covered glacier and its distinct morphology, particularly the differences in the eastern mountain face when compared to the Murfreit rock glacier.

In summary, the survey results reveal a dynamic situation at the Murfreit rock glacier, with ongoing permafrost degradation and a concerning observation of potential thawing after point 40 m (of the investigation line), raising the risk of dangerous debris releases. In contrast, the Piz Boé site exhibits stability attributed to its unique characteristics and mountain face morphology. To address these findings, further monitoring and safety measures are crucial for the Murfreit glacier, while ongoing research at the Piz Boé site could offer insights for mitigating permafrost-related risks in mountainous regions.

GPR Results

GPR is well-suited for glacial environments due to the favorable dielectric properties of ice and snow, which result in minimal signal attenuation [10]. The low dielectric constant of pure ice enables high-frequency radar signals (MHz range) to be transmitted with little attenuation. This allows for precise estimation of ice layer thickness, as the interface with the underlying bedrock (having a higher dielectric constant) produces a distinct reflection in the radargram.

Here in the following images in both profiles for Line 1 and Line 2. the signal attenuation within the snow layer is minimal, and distinct reflections are evident at the interface with the underlying frozen debris (indicated by the red dashed line) as well as at the boundary between the ice layer and the bedrock (represented by blue dashed lines).

The boundaries found in the GPR models are then used in the FDEM forward model. This involves taking the material boundaries seen in the GPR model and using them as information for the FDEM forward model. After creating the inverted FDEM model, we look at the same boundaries that were first spotted in the GPR model. Comparing them with the inverted FDEM demonstrates how well the FDEM model matches the GPR model. This comparison proves the effectiveness of the FDEM method in this study case and this type of low-resistivity environment.

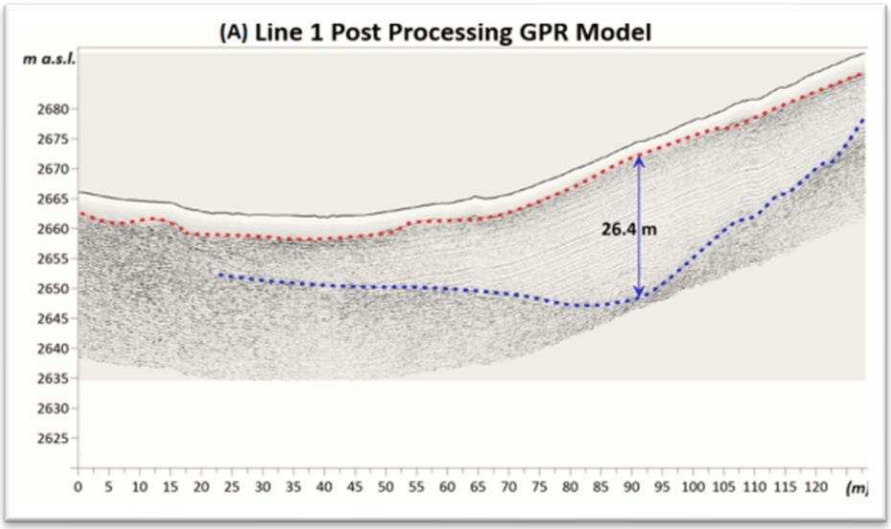

***Figure 48**: Interpretation of the GPR model Line 1 post-processing.*

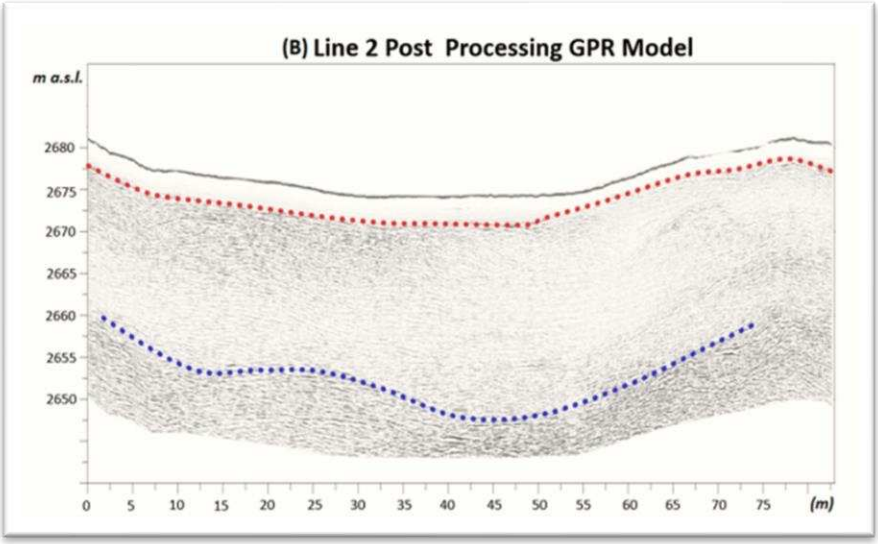

***Figure 49**: Interpretation of the GPR model Line 2 post-processing.*

The most significant ice thickness value (26.4 m—marked by the blue in Figure 48) is identified along Longitudinal Line 1, situated approximately 90 m from the profile's starting point. On-Line 2, variations in ice thickness are relatively minor; at the intersection with Line 1, the difference in thickness is negligible, measuring less than 10%. Notably, signal scattering of significance is observed in the profile's eastern section. This phenomenon suggests an increased presence of embedded debris and/or englacial water within the ice layer in this specific region.

FDEM results

The following image is the FDEM inverted image for Line 1 and Line 2. The inverted models for line 1 exhibit a relatively modest Root-Mean-Square Error (RRMSE) value of about 3.47% and for line 2 relatively high but acceptable value of 8%.

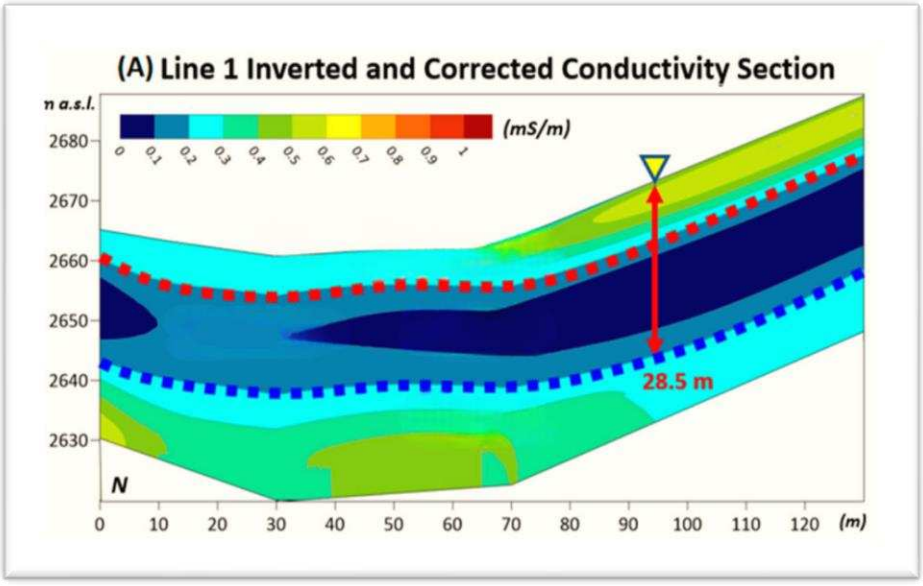

***Figure 50**.FDEM Inverted and corrected model line 1.*

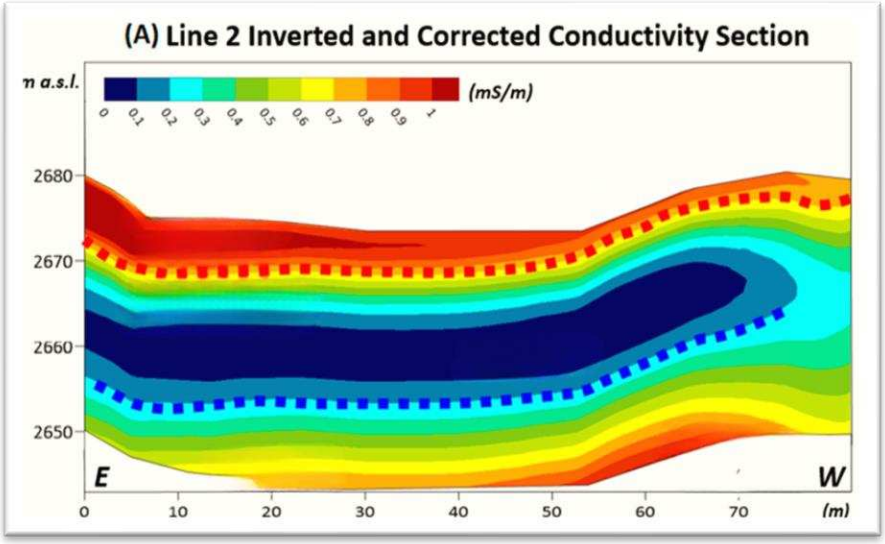

***Figure 51**.FDEM Inverted and corrected model line 2.*

As stated before, we know that sensitivity levels are higher closer to the surface and gradually diminish, essentially reaching zero at an approximate depth of 30 meters which is lower than the manufacturer's prediction. The reason for that is the FDEM investigation depth decreases in low electrical conductivity environments.

As we discussed in the previous chapter, forward modeling is crucial to making a model, especially in this type of low-conductivity environment. It is important to note that the limit of instrumental resolution (which is 0.1 mS/m for the CMD-DUO probe) is not considered in the forward modeling procedure.

Interpretation of the results

Although FDEM forward modeling did not consider any instrumental limit, the FDEM inverted model for Line 1 shows very similar results to the synthetic model (Figure 41), thanks to the shift in conductivity scales by two orders of magnitude.

The primary objective of our FDEM survey was not to reproduce the actual electrical conductivities of the subsurface layers, but rather to estimate the subsurface structure based on relative interpretations. The interpretation of the corrected FDEM conductivity sections is confirmed by the results of GPR surveys.

***Table 11**: Measured Conductivity Classification and Interpretation*

Conductivity Range (mS/m)	Interpretation
$< 1 \times 10^{-1}$	Ice-rich layer
1×10^{-1} - 2×10^{-1}	Ice-debris mixture
$> 2 \times 10^{-1}$	Unfrozen debris (top layers) or bedrock (bottom)
Close to 1	Upper snow cover layer

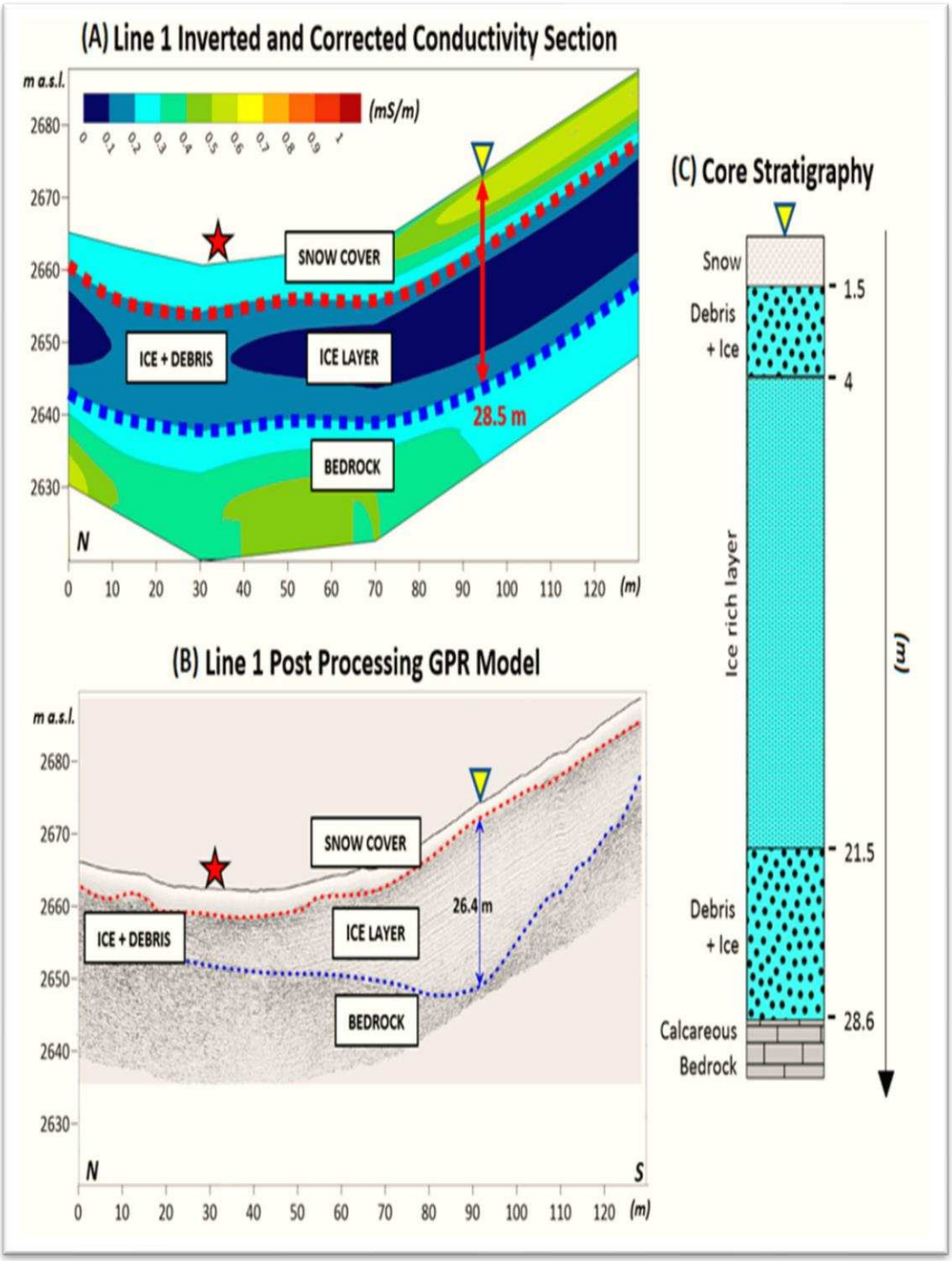

***Figure 52**.Comparison of Corrected Conductivity Profile (A) and GPR Model (B) for Line 1.*

The provided figures (Fig 52) display the delineation of boundaries between snow-layer-frozen debris and ice-layer bedrock using red-dashed and blue-dashed lines, respectively. The red star indicates the location of the snow cover thickness measurement in March 2022, while the yellow triangle signifies the April 2022 borehole drilling site. The borehole's internal structure is described in (C) with layers:

0–1.5 m snow cover, 1.5–4 m ice-debris mixture, 4–21.5 m ice-rich layer, 21.5–28.6 m ice-debris mixture, and 28.6 m bedrock. The same correction factor applied to Line 2's FDEM dataset aligns the ice-rich layer boundary to 1 × 10^-1 mS/m and the ice-debris mixture to 2 × 10^-1 mS/m. Similar alignment is observed between the corrected conductivity profile (Figure 52A) and the corresponding GPR model (Figure 52B) for Line 1.

- **FDEM Investigations on Line 1:**
- The inverted and corrected FDEM section (Figure 50) confirms the disappearance of the ice-rich layer ($\sigma < 0.1$ mS/m) near $x \approx 30$ m.
- Conductivity values between $0.1 < \sigma < 0.2$ mS/m in the middle layer ($x < 30$ m) suggest ice mixed with debris/englacial water.
- The maximum thickness of the ice layer seems to be at a distance of $x \approx 90–100$ m, and the boundary ice layer bedrock is defined at a depth of 28.5 m.
- The corrected FDEM section lacks the snow cover layer, due to the absence of VCP mode (s = 10m which focuses on shallow layers).

- **GPR profile Line 1**:
- The longitudinal GPR profile (Figure 52A) depicts a negative trend in the retreat of the Calderone Glacieret, indicating that the glacieret is getting smaller over time.
- Ice-rich layer was identified along the entire longitudinal GPR profile in 2015 by Monaco and Scozzafava, however, in our investigation in 2022 the ice-rich layer is disappearing at around $x \approx 30$ m (of our 135m long investigation line), which suggests a significant reduction in the presence of ice in this region over the seven-year period. this information agrees with the FDEM conductivity section.
- Maximum ice layer thickness at $x \approx 90$ m, boundary ice layer bedrock at 27.9 m.
- Stratigraphy from April 2022 drilling operations confirms the reliability of these results.
- The GPR model shows thinning of the ice layer towards the south, while FDEM's resolution is lower than GPR, exhibiting less evident thickness variation.
- The GPR model indicates a noticeable thickness increase (up to 5 m) of snow cover layer from South to North. This is then confirmed by drilling.

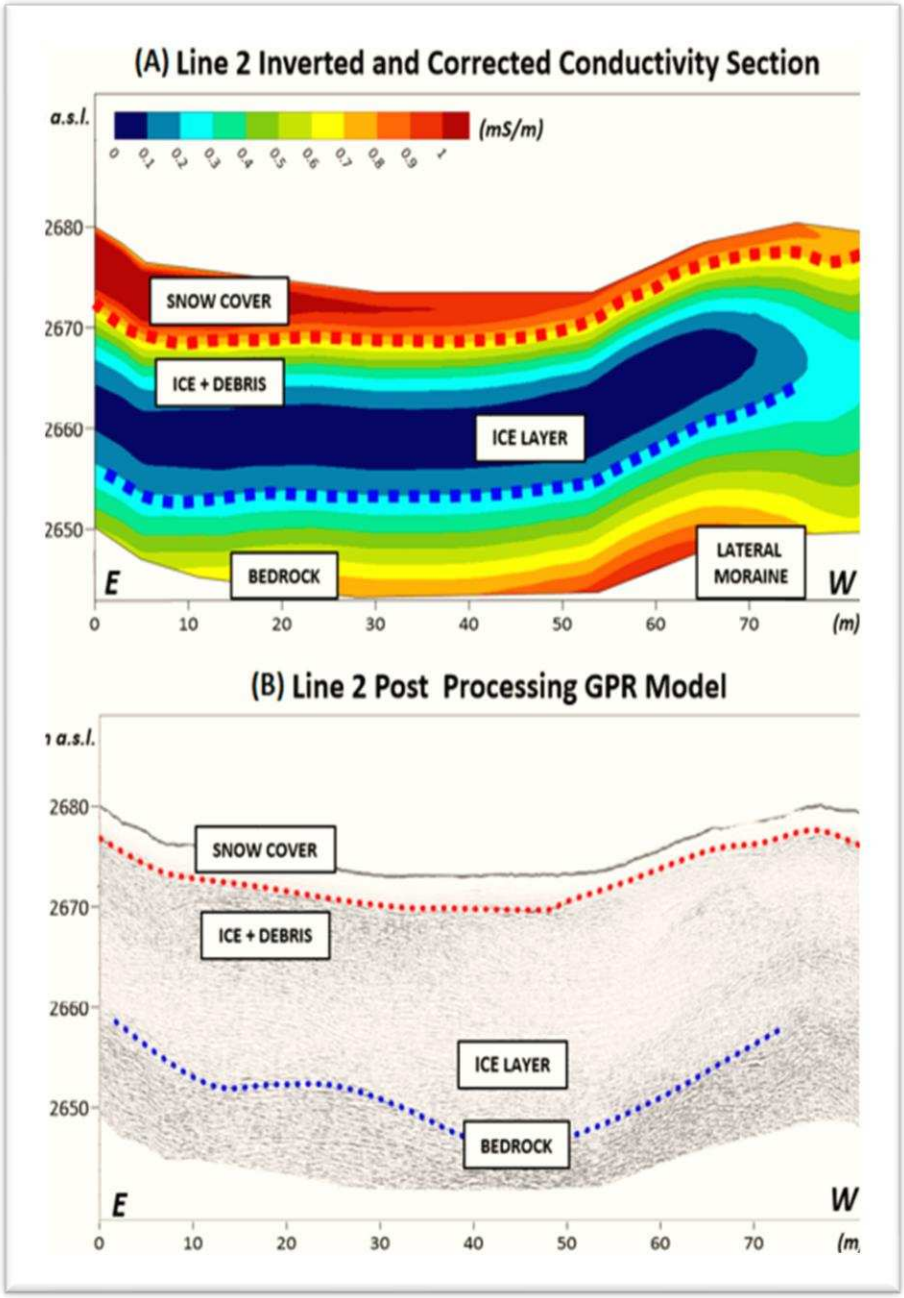

***Figure 53**. Line 2 displays the (A) adjusted and rectified electrical conductivity segment, along with the (B) ground-penetrating radar (GPR) model.*

In the given figures (fig.53) in both GPR and FDEM inverted models, the boundaries between the snow layer and frozen debris are illustrated by the red dashed line, while the boundary between the ice layer and bedrock is represented by a blue dashed line. As explained before, we used the boundary lines obtained by the GPR model(second image fig.53) in our FDEM forward model to be able to compare them properly and have a reference for our inverted conductivity model.

- **FDEM Investigations on Line 2:**
- There is a thickness increase of the snow cover layer from West to East. Here the dataset for VCP mode (s=10m) was correctly acquired (focusing on shallow layers).
  The corrected conductivity section (Figure 51) validates the thickness variation of the ice layer in Line 2.

- **GPR Investigations on Line 2:**
- GPR profile Line 2 (Figure 49) confirms the presence of the ice layer with a slightly lower maximum thickness compared to the longitudinal profile.
- The GPR model again indicates a noticeable thickness increase of the snow cover layer from West to East and a thicker ice layer in the western direction (50 < x < 60 m) of Line 2.

- **Integration and Analysis:**
- In comparison to the synthetic FDEM model (Figure 41), the corrected conductivity section shows higher values than expected for bedrock in the western direction, likely due to ice layer contact with lateral moraine.

As we can see here FDEM's inverted model is very similar to the GPR model which means that the FDEM CMD-DUO instrument was able to correctly determine the subsurface structure. The borehole realization that took place in April 2022 verified the model's findings and demonstrated that Integration of the GPR survey with the FDEM method enhances the characterization of glacieret structure and understanding of layer compositions.

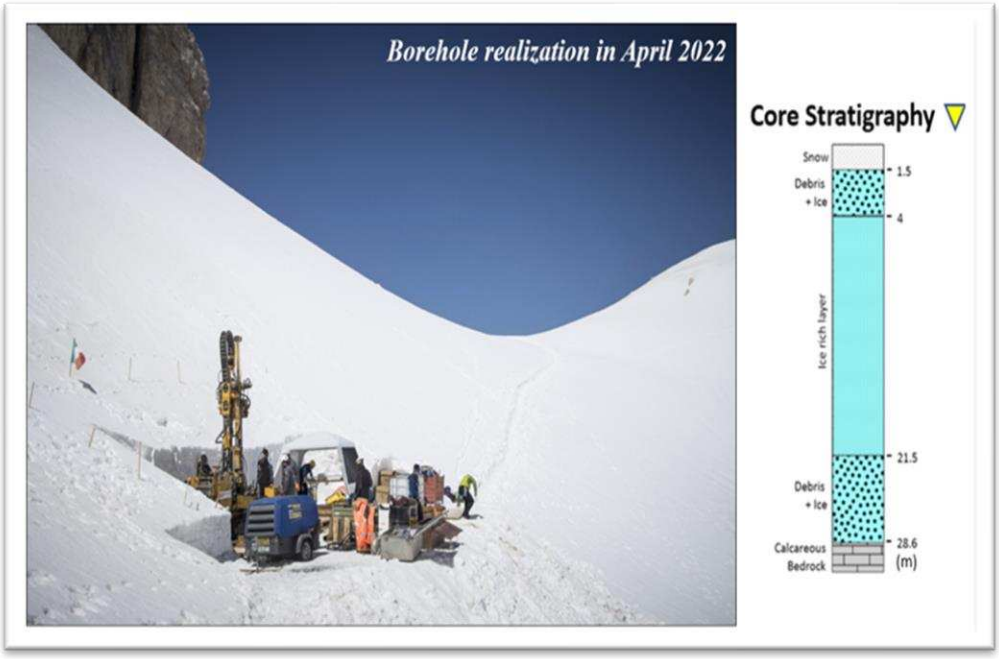

***Figure 54**. Borehole realization after geophysical investigations in Calderone glacieret (April 2022)*

Conclusion

To conclude, the purpose of this thesis was to demonstrate the great potential of FDEM as a technique for studying periglacial, glacial, and Rock glacier environments. In fact, FDEM surveys enabled us to evaluate the thickness of active layers (ALT) and characterize the glacier's structure without the need for galvanic contact with the ground. It also requires less logistical effort than other geophysical methods, such as ERT and seismic refraction techniques. These advantages become significant in high mountain environments where access is limited, and heavy equipment used in other geophysical methods may face challenges.

Regarding the Sella group mountain and the determination of active layer thickness, the ERT technique has shown its well-established ability to study these formations. Yet, it has some limitations, including time-consuming data acquisition, as it requires the placement of several electrodes and the measurement of resistivity using galvanic contact with the ground. It is essential to inject a sufficient amount of current into the ground in order to obtain a high-quality dataset (Salty water or conductive gel can be applied to the electrode locations in order to reduce the contact resistance). Helicopters are required for the transportation of cables and batteries to high mountain areas. Additionally, putting electrodes in the ground may not always be feasible in such environments. The preparation of the line, the acquisition phase, and the subsequent assembly of the line require considerable time and effort. As a result, this procedure is time-consuming and logistically challenging, especially for large-scale surveys or complex electrode arrays.

The FDEM method may not provide the same resolution as ERT, but it has proven its effectiveness. The results are very similar to those obtained by ERT. As stated, this technique offers advantages such as quick and easy data acquisition (it is lightweight and easily portable; it can be moved by a single individual) where heavy equipment of other geophysical methods may face limitations. Nevertheless, we should always aim at reducing calibration errors and ensuring data quality during surveys. Calibration errors are deviations between measured and true values that can arise from various sources, including instrumental drift, environmental factors, and operator-related issues.

In order to reduce the chances of obtaining scattered or noisy conductivity values, maintaining a fixed and constant probe distance from the ground is necessary. Ensuring that the probe remains parallel to the ground surface helps minimize orientation-related errors, shortening the survey time, and also helps minimize its impact on data quality. Surveying during periods with relatively stable air temperatures can decrease the error.

Moreover, we must underline the importance of prior information and forward modeling. It is important to choose the best-fit image that aligns with both the collected data and the predicted model from prior information. Filtering and smoothing can also help mitigate the inversion artifacts. Additionally, it should be noted that FDEM inversions may not provide as detailed and accurate results as the ERT technique. For these reasons, the combination of this method with the ERT method can provide a detailed map of the Murfreit and Piz Boé rock glaciers. To increase the speed and efficiency of investigation, the FDEM can be conducted as a preliminary survey to map wider areas of rock glaciers which defines the locations of interest to conduct ERT investigations.

Regarding the geophysical investigations performed on the Calderone Glacieret, GPR is a commonly used method in these frozen contexts, due to its small attenuation. By using this method, it was possible to accurately determine the exact thickness of the glacier and identify the boundaries between the ice layer and the calcareous bedrock with exceptional accuracy. By employing the FDEM forward modeling process and applying a correction factor to the inversion results of the field dataset, we overcame the limitation of instrumental resolution (0.1 mS/m). The inverted and calibrated FDEM model, supported by the results from the GPR data, proved the potential of the FDEM technique to be applied even in a low-conductive environment. Therefore, the integration of these two methods gave the Ice memory researchers the exact drilling position of the ice core.

These periglacial landforms present a more challenging GPR application since their coarse-blocky surfaces hinder data acquisition and intensify signal scattering. FDEM method is not affected by these scattering problems and is logistically more convenient; however, its resolution and accuracy are not as good as ERT. Therefore, it should be combined with GPR and used as a preliminary investigation technique in the same manner as in the Sella Mountain case, providing a better characterization of the subsurface structure and composition.

By gaining a deeper understanding of how glaciers respond to changing climatic conditions through the application of these geophysical techniques, it is possible to better estimate the vulnerabilities of glacial systems to climate change. These insights are crucial for climate models, predicting future climate scenarios, and developing effective strategies for mitigating climate change effects on glaciers and the broader environment.

In summary, by utilizing a combination of geophysical prospecting techniques with FDEM, it is possible to gain a detailed image of the subsurface characteristics of rock glaciers and glaciers. Each method has its advantages and limitations, and their integration allows for a more robust approach to periglacial environment research. These efforts contribute to our knowledge of glacial processes and dynamics, helping us address challenges related to climate change and glacial melting which is one of the world's most serious concerns at the moment.

References

[1] M. Qadri, 'EFFECTS OF GLOBAL WARMING ON THE ECONOMY'.

[2] European Environment agency, 'Global and European temperatures', *Global and European temperatures*, Jun. 22, 2022.

[3] E. (Katya) Uryupova, 'Climate Change and Geopolitics: Monitoring of a Thawing Permafrost', Mar. 2021.

[4] V.; Mair *et al.*, 'PermaNET-Permafrost Long-term Monitoring Network. Synthesis report', 2011, doi: 10.5167/uzh-59517.

[5] M. Pavoni, F. Sirch, and J. Boaga, 'Electrical and electromagnetic geophysical prospecting for the monitoring of rock glaciers in the Dolomites, northeast Italy', *Sensors (Switzerland)*, vol. 21, no. 4, pp. 1–18, Feb. 2021, doi: 10.3390/s21041294.

[6] M. Pavoni, J. Boaga, A. Carrera, S. Urbini, F. De Blasi, and J. Gabrieli, 'Remote Sens', vol. 15, 2023, doi: 10.3390/xxxxx.

[7] 'The Ice Core Record Past Archive of the Climate and Signpost to the Future'.

[8] P. Pandey, A. Ramanathan, and Gopalan Venkataraman, 'Remote Sensing of Mountain Glaciers and Related Hazards', in *Environmental Applications of Remote Sensing*, M. Marghany, Ed., Rijeka: IntechOpen, 2016, p. Ch. 5. doi: 10.5772/61917.

[9] K. Krainer, 'WP7 Water resources Action 7.2-Report Hydrological discharge measurements, geophysical measurements for assessing the ice content of permafrost phenomena', 2011.

[10] F. -Italy *et al.*, 'Field Trip Guidebook-P44 Triassic carbonate platforms of the Dolomites: carbonate production, relative sea-level fluctuations and the shaping of the depositional architecture Volume n° 5-from P37 to P54 English Desk-copy Editors: Eadie (Freelance indipendent professional) Acknowledgments'.

[11] K. Krainer, L. Mussner, M. Behm, and H. Hausmann, 'Multi-disciplinary investigation of an active rock glacier in the sella group (Dolomites; Northern Italy) Forensic Investigation of Pavement Distresses View project ALPSMOTION View project', 2020. [Online]. Available: https://www.researchgate.net/publication/283880404

[12] R. Brandner and L. Keim, 'A 4-DAY GEOLOGICAL FIELD TRIP IN THE WESTERN DOLOMITES Introduction and geological setting of the Dolomites', 2011.

[13] G. L. Cardello, 'Struttura del fianco occidentale del Massiccio del Gran Sasso d'Italia Einstein Telescope Sardinia: Geological and geophysical characterization View project', 2008, doi: 10.13140/RG.2.1.4799.5607.

[14] E. C. Casaccia, Le oscillazioni del ghiacciaio del Calderone (Gran Sasso d'Italia, Abruzzo - Italia centrale) e le variazioni climatiche degli ultimi 3000 anni, 2002.

[15] A. Monaco and M. Scozzafava, 'a preliminary survey for testing operativity and efficiency of gpr technology by means of unshielded antenna for the study of calderone glacier, central italy', 2017. [Online]. Available: http://amq.aiqua.it

[16] ‘Italy seeks to study, sample Europe’s southernmost glacier’.

[17] ALEX WOOD, ‘What is a Rock Glacier?’, 2012.

[18] *La revue de géographie alpine : année 2013 = Journal of alpine research : the year 2013.* Revue de géographie alpine, 2014.

[19] J. Noetzli, ‘Permafrost in Switzerland’, 2008. [Online]. Available: http://www.permos.ch

[20] ‘World Heritage Glaciers Sentinels of climate change’, 2022, doi: 10.3929/ethz-b-000578916.

[21] W. H. Johnson, ‘Pleistocene Epoch’, *Encyclopedia Britannica*. 2023.

[22] K. Grunewald and J. Scheithauer, ‘Europe’s southernmost glaciers: Response and adaptation to climate change’, *Journal of Glaciology*, vol. 56, no. 195, pp. 129–142, Apr. 2010, doi: 10.3189/002214310791190947.

[23] L. D’Alessandro, M. D’Orefice, M. Pecci, C. Smiraglia, and R. Ventura, ‘The Strong Reduction Phase of the Calderone Glacier During the Last Two Centuries: Reconstruction of the Variation and of the Possible Scenarios With GIS Technologies’, in *Global Change and Protected Areas*, G. Visconti, M. Beniston, E. D. Iannorelli, and D. Barba, Eds., Dordrecht: Springer Netherlands, 2001, pp. 425–433. doi: 10.1007/0-306-48051-4_39.

[24] E. Branda, B. Turchetti, G. Diolaiuti, M. Pecci, C. Smiraglia, and P. Buzzini, ‘Yeast and yeast-like diversity in the southernmost glacier of Europe (Calderone Glacier, Apennines, Italy)’, *FEMS Microbiol Ecol*, vol. 72, no. 3, pp. 354–369, Jun. 2010, doi: 10.1111/j.1574-6941.2010.00864.x.

[25] R. J. Durrheim, M. S. D. Manzi, and S. J. Webb, ‘Exploration Geophysics’, in *Encyclopedia of Geology (Second Edition)*, D. Alderton and S. A. Elias, Eds., Oxford: Academic Press, 2021, pp. 219–234. doi: https://doi.org/10.1016/B978-0-12-409548-9.12536-9.

[26] ‘NEET_CHAPTER_WISE_TOPIC_WISE_SOLVED_PAPE’.

[27] Z. M. Sbartaï, S. Laurens, J. Rhazi, J. P. Balayssac, and G. Arliguie, ‘Using radar direct wave for concrete condition assessment: Correlation with electrical resistivity’, *J Appl Geophy*, vol. 62, no. 4, pp. 361–374, Aug. 2007, doi: 10.1016/j.jappgeo.2007.02.003.

[28] S. Kowalczyk, K. A. Zukowska, M. J. Mendecki, and D. Łukasiak, ‘Application of electrical resistivity imaging (ERI) for the assessment of peat properties: A case study of the Całowanie Fen, Central Poland’, *Acta Geophysica*, vol. 65, no. 1, pp. 223–235, Mar. 2017, doi: 10.1007/s11600-017-0018-9.

[29] S. Hemeda, ‘Electrical Resistance Tomography (ERT) Subsurface Imaging for Non-destructive Testing and Survey in Historical Buildings Preservation’, *Aust J Basic Appl Sci*, vol. 7, no. 1, pp. 344–357, 2013, [Online]. Available: www.agiusa.com

[30] C. Hauck Zurich and D. H-E Minor, ‘VAW Mitteilung 171: Geophysical methods for detecting permafrost in high mountains’, 2001.

[31] B. Sanfilipo, ‘Passive and Active Low-Frequency Electromagnetic Spectroscopy for’ Airborne Detection of Underground Facilities Prepared for’, 1998.

[32] P. Kinsler, ‘Faraday’s Law and Magnetic Induction: Cause and Effect, Experiment and Theory’, *Physics (College Park Md)*, vol. 2, no. 2, pp. 150–163, 2020, doi: 10.3390/physics2020009.

[33] V. Marghussian, '4 - Magnetic Properties of Nano-Glass Ceramics', in *Nano-Glass Ceramics*, V. Marghussian, Ed., Oxford: William Andrew Publishing, 2015, pp. 181–223. doi: https://doi.org/10.1016/B978-0-323-35386-1.00004-9.

[34] 'The spatial characterisation of contaminant distribution found at industrial sites using combined geophysical / hydrogeological fieldstudies and laboratory modelling', 2012, doi: 10.13140/2.1.3707.2648.

[35] J. B. Callegary, T. P. A. Ferré, and R. W. Groom, 'Vertical Spatial Sensitivity and Exploration Depth of Low-Induction-Number Electromagnetic-Induction Instruments', *Vadose Zone Journal*, vol. 6, no. 1, pp. 158–167, Feb. 2007, doi: 10.2136/vzj2006.0120.

[36] D. Beamish, 'Low induction number, ground conductivity meters: A correction procedure in the absence of magnetic effects', *J Appl Geophy*, vol. 75, no. 2, pp. 244–253, Oct. 2011, doi: 10.1016/j.jappgeo.2011.07.005.

[37] 'EM current measurement at low induction number'.

[38] J. Boaga, 'The use of FDEM in hydrogeophysics: A review', *J Appl Geophy*, vol. 139, pp. 36–46, Apr. 2017, doi: 10.1016/J.JAPPGEO.2017.02.011.

[39] F. C. Moura de Andrade and T. Fischer, 'Generalised relative and cumulative response functions for electromagnetic induction conductivity meters operating at low induction numbers', *Geophys Prospect*, vol. 66, no. 3, pp. 595–602, Mar. 2018, doi: 10.1111/1365-2478.12553.

[40] P. McLachlan, G. Blanchy, and A. Binley, 'EMagPy: Open-source standalone software for processing, forward modeling and inversion of electromagnetic induction data', *Comput Geosci*, vol. 146, Jan. 2021, doi: 10.1016/j.cageo.2020.104561.